Case Studies in Thermal Engineering 61 (2024) 104973

Contents lists available at ScienceDirect

Case Studies in Thermal Engineering

journal homepage: www.elsevier.com/locate/csite

Multi-objective optimization and artificial neural network models for enhancing the overall performance of a microchannel heat sink with fins inspired Tesla valve profile

Longyi Ran[a], Samah G. Babiker[b,c], Pradeep Kumar Singh[d,*], Mohammed A. Alghassab[e,**], Ngoc Vu-Thi-Minh[f,****], Myasar mundher adnan[g,o,p], Salah Knani[h], Hakim AL Garalleh[i], Albara Ibrahim Alrawashdeh[j,k], Fawaz S. Alharbi[l], Hadil faris Alotaibi[m], Fahid Riaz[n,***]

[a] Chongqing Chemical Industry Vocational College, Chongqing, 401228, China
[b] Department of Basic Science, Preparatory Year, Prince Sattam bin Abdulaziz University, Al-Kharj, 11942, Saudi Arabia
[c] Department of Electronic Physics, Faculty of Applied Science, Red Sea University, Port Sudan, 33311, Sudan
[d] Department of Mechanical Engineering, Institute of Engineering & Technology, GLA University, Mathura, U.P., 281406, India
[e] Electrical Engineering Department, College of Engineering, Shaqra University, Riyadh, 11911, Saudi Arabia
[f] School of Economics and International Business, Foreign Trade University, Hanoi, Viet Nam
[g] College of technical engineering, The Islamic University, Najaf, Iraq
[h] Department of Physics, College of Science, Northern Border University, Arar, Saudi Arabia
[i] Department of Mathematical Science, College of Engineering, University of Business and Technology, Jeddah, 21361, Saudi Arabia
[j] Department of General Subjects, College of Engineering, University of Business and Technology, Jeddah, 21361, Saudi Arabia
[k] Department of Chemistry and Chemical Technology, College of Science, Tafila Technical University, Tafila, 66110, Jordan
[l] Department of Mechanical Engineering, College of Engineering, University of Hafr Al Batin, P.O. Box 1803, Hafr Al Batin, 39524, Saudi Arabia
[m] Department of Pharmaceutical Sciences, College of Pharmacy, Princess Nourah bint AbdulRahman University, Riyadh, 11671, Saudi Arabia
[n] College of Engineering, Abu Dhabi University, Abu Dhabi, United Arab Emirates
[o] College of technical engineering, The Islamic University of Al Diwaniyah, Al Diwaniyah, Iraq
[p] College of technical engineering, The Islamic University of Babylon, Babylon, Iraq

ARTICLE INFO

Keywords:
Heat dissipation
Artificial neural network
Microchannel heat sink
Fin configuration
Tesla valve
Thermal analysis

ABSTRACT

Microchannel heat sinks (MCHSs) are advanced cooling systems used in various applications such as electronics cooling, thermal management of high-power microprocessors, and microelectronic devices. These heat sinks are designed to efficiently dissipate heat generated by electronic components to maintain optimal operating temperatures and ensure device reliability. Employing appropriate fins within MCHSs is a crucial strategy to enhance heat removal efficiency. Since few investigations have been performed on the simultaneous thermo-hydraulic features in microchannels with Tesla valves, this research addresses this gap by suggesting that the microchannels of a heat sink be reinforced with novel Tesla valve-shaped fins. Tesla valves are designed to offer different levels of resistance depending on the flow direction. This characteristic allows for selective control of pressure drop and heat transfer efficiency by simply switching the flow direction. Utilizing Tesla valve-shaped fins is an almost new approach that differentiates the current

* Corresponding author.
** Corresponding author.
*** Corresponding author.
**** School of Economics and International Business, Foreign Trade University, Hanoi, Vietnam
E-mail addresses: pradeep.kumar@gla.ac.in (P.K. Singh), malghassab@su.edu.sa (M.A. Alghassab), vuminhngoc@ftu.edu.vn (N. Vu-Thi-Minh), fahid.riaz@adu.ac.ae (F. Riaz).

https://doi.org/10.1016/j.csite.2024.104973
Received 10 April 2024; Received in revised form 18 July 2024; Accepted 12 August 2024
Available online 15 August 2024

research from conventional designs. The advantage of this structure is that under different circumstances, depending on whether more heat transfer is required or less pressure drop (ΔP), the flow direction can be changed, and the maximum efficiency of the MCHS can be accessed. The other innovative aspect of this study lies in the integration of artificial neural network (ANN) models to optimize the efficiency of MCHSs equipped with Tesla valve-shaped fins. The simulations were conducted to characterize the flow and thermal features of the MCHS. Then, these data were used as the benchmark for training the ANN models. Four ANN models were introduced to anticipate the Nusselt number (*Nu*) and ΔP in each forward and reverse direction. The divider's acute angle (α), the divider's obtuse angle (β), and the divider's radius (R) were selected as the input data. Multi-objective optimization and genetic algorithms were used to achieve the optimal conditions. In the optimal thermal design (Setting 2: MCHS with fin variables of $\alpha = 60$ $\beta = 180$, and $R = 80$ μm in reverse flow direction), the overall performance had a significant enhancement of 57.1 % compared to the device lacking fins. Furthermore, in Setting 2, the overall performance of the MCHS and its diodicity experienced notable improvements of approximately 12.1 % and 38.5 %, respectively. Implementing the parameters of Setting 5 (MCHS with fin variables of $\alpha = 60$, $\beta = 152.32$, and $R = 73.10$ μm in forward direction) during fin production resulted in a notable enhancement of about 41.1 % in the device's overall performance.

Nomenclature

A_c	inlet cross section area (m^2)	r	response
A_{hf}	heat flux area (m^2)	T	temperature (K)
A_{ht}	heat transfer area (m^2)	U	velocity (m/s)
b	bias	W	weight
C_p	heat capacity (J/kg.K)		
D_h	hydraulic diameter (m)	Symbols	
Di	diodicity	α	the acute angle of the divider (degree)
f	friction factor	β	the obtuse angle of the divider (degree)
h	heat transfer coefficient	ρ	density (kg/m^3)
I	input of neuron	μ	dynamic viscosity (Pa.s)
k	thermal conductivity (W/m.K)		
m	number of tests	Subscripts	
N	number of neurons	b	basic
n	number of input variables	f	forward direction
ΔP	pressure drop (Pa)	fl	fluid
q	heat transfer rate (W/m^2)	HL	hidden layer
Q	heat absorbed by water	OL	output layer
R	divider's radius (m)	r	reverse direction
R_t	total thermal resistance (K/W)	s	solid
REI	relative efficiency index		
$REIR$ relative efficiency index ratio			

1. Introduction

Technology has considerably impacted modern life, and the development trend has been toward making technology smaller, faster, more powerful and having efficient manufacturing supply chain [1]. One of the important aspects of manufacturing logistics is miniaturization of electronic products which has allowed engineers to fit more computing power into smaller spaces, while the increased power has enabled them to do more with the same amount of resources [2]. The high power of microelectronic equipment is associated with remarkable heat generation, which can damage their circuits in multiple ways [3]. High temperatures can affect the electrical properties of semiconductor materials, leading to reduced performance. Maintaining optimal operating temperatures ensures that electronic devices perform reliably [4]. Failures due to poor thermal management can lead to increased warranty claims and higher costs for manufacturers. The ongoing challenges in thermal management drive innovation in cooling technologies. Advancements in materials science and cooling techniques, such as heat sinks, are direct responses to these challenges [5].

Tuckerman and Pease [6] are recognized as innovators in applying microchannel heat sinks (MCHSs) for electronics cooling. MCHSs are designed to enlarge the surface area of the heat sinks, allowing for more efficient heat transfer [7]. They have become increasingly popular for cooling high-powered electronics due to their small size, low weight, and ability to dissipate heat quickly and efficiently [8,9]. After Tuckerman and Pease, some research has focused on improving the physical design of the MCHSs, such as optimizing the shape or size of channels, utilizing fins or cavities, and adding lugs or dimples to raise the surface area and ameliorating heat transfer [10,11]. Other research has looked into improving the material used in these devices, such as switching from metal to ceramic or nanofiber coatings, to improve their performance [12]. For instance, Haque et al. [13] analyzed the role of several configurations of lozenge pin-fins within an MCHS. Different aspect ratios of these fins were examined to amend the efficiency of the system. The most significant increase in the *Nu* was seen when the aspect ratio of lozenge-shaped pin-fins was 1.00. At this aspect ratio, the *Nu* ranged from 7.12 to 15.26. Yang et al. [14] optimized the efficiency of an MCHS reinforced with secondary oblique microchannels. They used newly developed techniques like response surface methodology (RSM) and genetic algorithm (GA) to maximize the thermo-hydrodynamic features of the system. According to their data, the hybrid design could decrease the thermal resistance (approximately 18.83 %) of manifold MCHS. Lu et al. [15] proposed utilizing high thermal conductivity substances like diamond/copper composites within the channels of an MCHS. They changed the number of channels to obseve its impact on the thermal behavior of the system. Based on their findings, the highest *Nu* was 29.7 and the lowest thermal resistance was 0.119 K/W. Their proposed device could successfully eliminate the significant heat flux of 400 W/cm^2 from the surface of the chip. Zhang et al. [16] examined the structure parameters and arrangement ways of internal fins in the channels of an MCHS. They reported that compared to the device with straight channels, the optimized model's maximum temperature and pumping power were reduced by about 6.67 % and 13.33 %, respectively. Singupuram et al. [17] introduced a unique configuration of an MCHS to keep the temperature of the chip in a safe zone. The device passage was altered by adding circular extruding ribs to its side wall. The study examined the impact of these ribs with sector angles between 45° and 80°. The highest *Nu*, ranging from 7.26 to 64.11, was observed at a sector angle of 80° for the mentioned ribs. Utilizing computational fluid dynamics, Polat et al. [18] evaluated the role of different pin-fin designs on the hydrodynamic properties of an MCHS. They understood that the diamond-shaped pin fins considerably increased the thermal features of the heat sink at an enhanced ΔP ratio. Heat transfer behavior and hydrodynamic properties of a microchannel with dimples and fillet profile were examined by Okab et al. [19]. They found that employing dimples in the sidewalls of the microchannels and fillet profiles in their basal wall led to a considerable increment in the thermal characteristics of the MCHS. *Nu* of the device enhanced by about 60 % compared to the simple microchannels (without dimples and fillet profile).

Given the various investigation performed in MCHSs, the shape of fins or complex structures (like ribs or grooves) of the microchannels changes the flow dynamics, impacting the heat transfer coefficients [20,21]. The presence of ribs or grooves promotes better mixing of the fluid. This disrupts the thermal boundary layer and enhances convective heat transfer, leading to more efficient cooling [22]. They can induce turbulence in the fluid flow which has higher heat transfer coefficients because it enhances the mixing of hot and cold fluid regions [23]. Fin shapes also have a remarkable influence on the ΔP of the MCHSs, which can impact the device's total performance [24]. Furthermore, the amount of fins, angle, and fin spacing can affect the function of these heat sinks [25]. While increasing the number of fins enhances heat transfer, it also introduces greater flow resistance. This results in a higher ΔP across the microchannels, which can lead to increased energy consumption for pumping the coolant through the system [26]. Hence, ongoing research aims to develop novel fin shapes that strike a balance between maximizing heat transfer and minimizing pressure drop. Innovative designs and geometries are explored to optimize the thermal performance without significantly increasing the flow resistance [27]. High ΔP in channels is caused by several factors, including small channel diameter, high Reynolds number, and high surface roughness [28]. It can lead to lower flow rates and unfavorable performance of the MCHSs [29,30]. To reduce the ΔP in MCHSs, it is essential to optimize the design of the device, such as utilizing appropriate fins, to achieve the desired flow rate [31]. Another suggested technique for diminishing the ΔP is using flow control devices like Tesla valves [32].

As a type of one-way valve, Tesla valves are designed to provide a precise and consistent flow rate, even in extreme conditions [33]. These valves can also control the pressure of the fluid to ensure optimal performance [34,35]. In addition, they are highly reliable and provide a low-cost solution for managing ΔP. Tesla valves are often used in the automotive, aerospace, heat exchangers, cooling of batteries, and energy industries [36,37]. Recently, the design of the Tesla valve has been proposed to apply within the microchannels, owing to its mechanism of increasing fluid mixing degree to a large extent [38]. Sun et al. [39] explored the thermo-hydraulic features of an MCHS with three various structures of microchannels. They observed that using microchannels with Tesla valves, microchannels with sector bump, and microchannels with diamond bump caused a noticeable increment in the *Nu* of the MCHS compared to the heat sink with straight channels. Based on their findings, the microchannels with Tesla valves provided higher thermal performance because of the intensified fluid mixing. Zhang et al. [40] altered the geometrical parameters of a Tesla valve and investigated their role in the overall performance of the equipment. Based on their findings, when the parameters of diverting Angle, stages, and bend outlet width enhanced, the diodicity value rose significantly. They noticed that changing the number of stages had a remarkable impact on the flow characteristics of the Tesla valve in both forward and reverse directions. Fan et al. [41] examined the heat dissipation, maximum temperature, and ΔP in lithium-ion batteries via a Tesla valve with multi stages (as an MCHS) and phase change materials. They understood that applying the Tesla valve and phase change material within these batteries decreased the energy consumption needed for fluid flow by about 79.9 % compared with the traditional batteries. Li et al. [42] recommended to add an arch channel within each stage of a Tesla valve to amend the device's performance. They applied multi-objective optimization and RSM to find the best solutions. The authors pointed out that the flow resistance ratio enhanced by about 8.7 % copared to the original Tesla valve (without arch channels). At lower inlet pressures, the rise in flow resistance ratio was about 1.4 % greater compared to that at higher inlet pressures. According to the literature, while extensive research has been devoted to enhancing heat transfer in MCHSs, only a few studies have focused on developing MCHSs with adjustable pressure drop mechanisms.

Manufacturing MCHSs and conducting experimental studies to investigate their performance are often costly [43]. Numerical methods are used to simulate and model a wide variety of physical phenomena accurately; however, they require complex computations and often involve multiple variables and parameters [44,45]. In contrast, statistical procedures such as artificial neural networks (ANNs) or RSM are generally better choices than numerical and experimental methods because they are less time-consuming and require less computing power [46]. Additionally, statistical methods are not limited by the accuracy of physical measurements, as is the case with numerical and experimental methods [47]. Li et al. [48] optimized the flow and thermal performances of a disk-shaped MCHS exerting ANN and RSM. Based on their findings, the *Nu* and ΔP values predicted by the ANN model were similar to those acquired via the numerical simulation. Furthermore, the mentioned models proposed the best values of geometrical parameters for the microchannels, which could increase the efficiency index (the balance state between the *Nu* and ΔP) by about 3.85 %. Vaferi et al. [49] evaluated the role of structural parameters and the inlet Reynolds number in the effectiveness of a Tesla valve. They utilized ANN models to find the optimal designs. Pressure drop and temperature difference were the responses in the applied ANN models.

The best pressure drop was 4.581, signifying a 358.1 % enhancement in pressure drop in the reverse direction compared to that of forward direction. The optimal temperature difference was determined to be 1.862. Xie et al. [50] evaluated the hydrodynamic and thermal behavior of a heat exchanger with vortex generators applying ANN. They picked out three geometric parameters of the vortex generators to study their effects on the effectiveness of the device. It was found that the ANN models proposed reducing the attack angle and increasing the arc angle to achieve a higher overall performance of the device. Kou et al. [51] proposed a unique-designed Tesla valve to optimize hydrogen flow. They altered the structural parameters of the valve in pre-defined ranges and assessed their impact on the flow regulation efficiency of the device. According to their outcomes, the newly designed Tesla valve raised the pressure drop by approximately 4830 % and 1354 % in reverse and forward directions in comparison with the bend-free channels.

According to the literature review, few investigations have been performed on the simultaneous thermo-hydraulic features in microchannels with Tesla valves. This research addresses this gap by suggesting that the microchannels of a heat sink be reinforced with novel Tesla valve-shaped fins. The design of Tesla valves inherently creates a low-resistance path in the forward direction of fluid flow. By aligning the fins in a manner that facilitates this low-resistance path, the pressure drop across the microchannels can be minimized, maintaining efficient cooling without excessively burdening the pump. Besides, Tesla valve-shaped fins provide a larger surface area compared to traditional straight fins. This increased surface area enhances heat transfer between the fluid and the fins. The unique shape of Tesla valve fins induces turbulence in the fluid flow, which enhances convective heat transfer. While promoting turbulence, the Tesla valve-shaped fins can be designed to minimize flow resistance, maintaining an optimal balance between pressure drop and heat transfer enhancement. Tesla valves are designed to offer different levels of resistance depending on the flow direction. This characteristic allows for selective control of pressure drop and heat transfer efficiency by simply switching the flow direction. Utilizing Tesla valve-shaped fins is an almost new approach that differentiates the current research from conventional designs. The other innovative aspect of this study lies in the integration of ANN models to optimize the efficiency of MCHSs equipped with Tesla valve-shaped fins. Specifically, four ANN models are introduced to anticipate the Nu and ΔP in both forward and reverse flow directions. This dual approach not only enhances the thermal management capabilities of MCHSs but also provides a predictive framework for their performance, marking a significant advancement in the field of thermal management technologies. The best configuration of the fins within the microchannels is detected by examining the three structural parameters (the acute angle of the divider, the obtuse angle of the divider, and the radius of the divider) of the Tesla valve-shaped fins. The outcomes of the present investigation can be a rich reference for researchers who are intrigued by this particular field.

2. Methodology

2.1. Physical model

The multi-nozzle MCHS, which has been analyzed in the numerical research of Tran et al. [52], is elected to be examined in this work. The selected device consists of several microchannels, while each microchannel has a top cover, inlet and outlet sections, and substrate (as demonstrated in Fig. 1a). The top cover operates as a hindrance to stop the direction of the fluid flow from being altered.

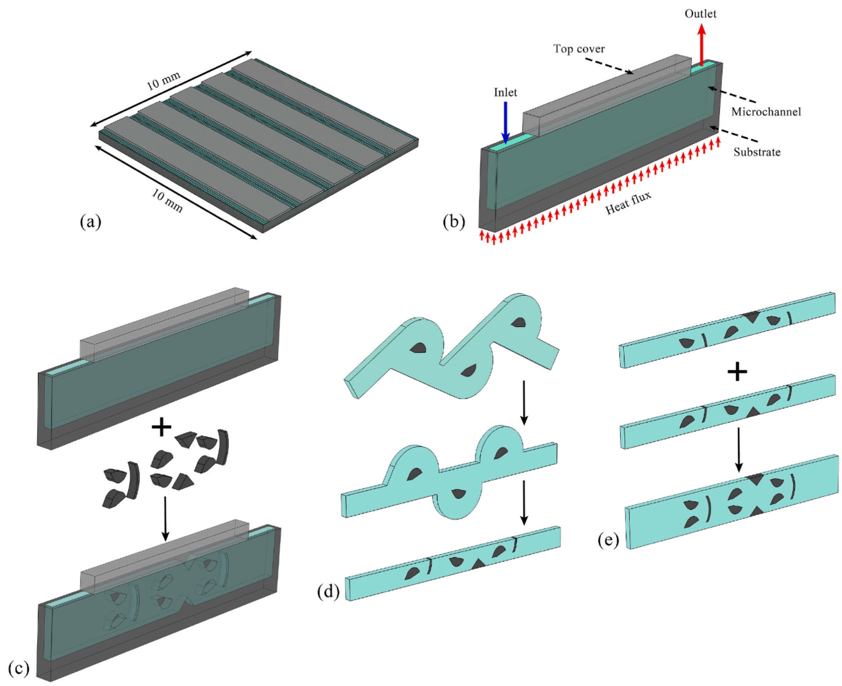

Fig. 1. Geometric model of (a) the selected MCHS and (b) a microchannel [52]. (c) schematic diagram of the microchannel with Tesla valve-shaped fins, the evolution process of (d) the Tesla valve, and (e) microchannels used in the current work.

Based on the geometrical symmetry and to reduce the amount of time needed for computations, a single microchannel with its top cover and substrate is set as the simulated domain (Fig. 1b). Then, inspiring the structure of the Tesla valves, various fins are designed to be employed within the microchannels to boost the heat transfer. Some changes are applied to the geometry to fit the fins inside the microchannels, and the channels' length is considered larger. A 3D model of the modified microchannel design in a schematic form is indicated in Fig. 1c. Besides, the evolution process of the Tesla valve used herein is represented in Fig. 1d. Based on this figure, some fins are embedded inside half part of a microchannel. In contrast, the other fins with the same configuration are added inversely into another half of the microchannel. Combining these fins within the microchannel, a new fin design is created, making the channel act like a Tesla valve. Three types of dividing fins, curved fins, and triangular-shaped fins existed in this design. Each of these fins causes a part of the operation of the Tesla valve. For example, when the coolant flows into the MCHS in the reverse direction, most of the inlet flow is directed to the center of the channel by the dividers. Then, the passing fluid hits the curved fins and causes a ΔP, creating vortices in this area. This can cause more fluid mixing and increase heat transfer. After that, the fluid enters the next stage and experiences the opposite of this, that is, the fluid is pushed by the dividers from the center to the walls. Finally, by hitting the triangular-shaped fins, it is directed back to the center of the channel and again to the dividers and curved fins. The goal is to achieve a heat sink that can have more heat transfer with a minimized ΔP, and for the times when high ΔP is required, it can act as a non-return valve and produce a significant ΔP in the reverse direction. The Tesla valve structure can be optimized to minimize pressure loss while still enhancing heat transfer, making it an efficient design choice for MCHSs. The compact design of Tesla valve-shaped fins allows for a higher density of fins within a given volume, increasing the heat sink's capacity without significantly increasing its size. Fig. 2 illustrates the geometrical parameters of these microchannels together with their fins. Among the different parameters, the acute angle of the divider (α), the obtuse angle of the divider (β), and the radius of the divider (R) are selected as the input data, which are used later to optimize the effectiveness of the system. These parameters are varied within specific ranges to study their effects on the responses. The other structural parameters of the microchannels remain constant throughout the simulation process. The top cover and substrate of the microchannels are made of polymethyl methacrylate and silicon materials. Water is the working fluid passing through these channels.

2.2. Mathematical model

The flow regime within microchannels is generally laminar due to the small dimensions of the channels. In this investigation, the Re at the inlet is set at 200, and the fluid flow does not reach even into the early stages of the transitional regime at this *Re*. Therefore, the laminar flow condition can be taken into account. Conjugate heat transfer is employed to determine the thermal behavior in the solid and fluid domains of the MCHS, as well as the energy exchange between these two parts. Furthermore, conservation equations are utilized to describe the physical laws governing the flow and to specify the hydrodynamic features of the system. COMSOL Multiphysics is exerted to model the thermo-hydrodynamic properties of MCHS using the finite element method. It is important to note that without boundary conditions, the numerical simulations could not apply the differential equations to the simulated model. Thus, various assumptions and boundary conditions are considered below to reduce the complexity of the equations and provide the needed information at the boundaries.

- Steady condition for simulations
- Incompressible and single-phase fluid
- Non-slip and No-temperature-jump at solid-fluid interfaces
- Thermal symmetry at the side walls
- Insignificant temperature difference in the fluid and constant features for the materials (Table 1)
- Constant inlet velocity of 2.35 m/s ($Re_{in} = 200$) and water flow temperature of 293 K
- Outlet pressure of 0

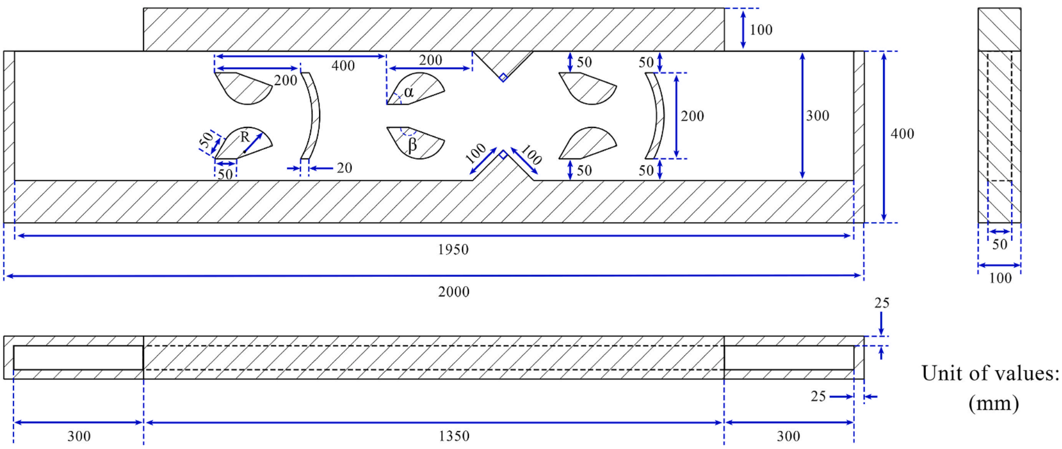

Fig. 2. Geometrical parameters of a microchannel with Tesla valve-shaped fins.

Table 1
Properties of the materials at 293 K.

Properties	Water [53]	Silicon [54]	Polymethyl Methacrylate [52]
ρ	998.2	2330	1420
k	0.6	148	0.19
C_p	4182	702	1960
μ	1.003×10^{-3}	–	–

- Heat flux of 200 W/cm^2
- Neglected gravity effects and radiation

It is worth mentioning that in this study, the goal is to obtain the best design for the MCHS by applying fins and optimizing the geometry of the fins. For this reason, the parameters of the boundary conditions such as velocity, heat flux, and temperature were assumed to be constant so that only the influence of the geometry is highlighted. Adopting the abovementioned simplifications, the formulations of the conservation equations are outlined as follows [55,56]:

$$\rho_{fl}\left(\frac{\partial U_x}{\partial x}+\frac{\partial U_y}{\partial y}+\frac{\partial U_z}{\partial z}\right)=0 \tag{1}$$

$$\rho_{fl}\left(U_x\frac{\partial U_x}{\partial x}+U_y\frac{\partial U_x}{\partial y}+U_z\frac{\partial U_x}{\partial z}\right)=-\frac{\partial P}{\partial x}+\mu\left(\frac{\partial^2 U_x}{\partial x^2}+\frac{\partial^2 U_x}{\partial y^2}+\frac{\partial^2 U_x}{\partial z^2}\right) \tag{2}$$

$$\rho_{fl}\left(U_x\frac{\partial U_y}{\partial x}+U_y\frac{\partial U_y}{\partial y}+U_z\frac{\partial U_y}{\partial z}\right)=-\frac{\partial P}{\partial y}+\mu\left(\frac{\partial^2 U_y}{\partial x^2}+\frac{\partial^2 U_y}{\partial y^2}+\frac{\partial^2 U_y}{\partial z^2}\right) \tag{3}$$

$$\rho_{fl}\left(U_x\frac{\partial U_z}{\partial x}+U_y\frac{\partial U_z}{\partial y}+U_z\frac{\partial U_z}{\partial z}\right)=-\frac{\partial P}{\partial z}+\mu\left(\frac{\partial^2 U_z}{\partial x^2}+\frac{\partial^2 U_z}{\partial y^2}+\frac{\partial^2 U_z}{\partial z^2}\right) \tag{4}$$

$$\rho_{fl}C_p\left(U_x\frac{\partial T_{fl}}{\partial x}+U_y\frac{\partial T_{fl}}{\partial y}+U_z\frac{\partial T_{fl}}{\partial z}\right)=k_{fl}\left(\frac{\partial^2 T_{fl}}{\partial x^2}+\frac{\partial^2 T_{fl}}{\partial y^2}+\frac{\partial^2 T_{fl}}{\partial z^2}\right) \tag{5}$$

$$k_s\left(\frac{\partial^2 T_s}{\partial x^2}+\frac{\partial^2 T_s}{\partial y^2}+\frac{\partial^2 T_s}{\partial z^2}\right)=0 \tag{6}$$

In Eqs. (1)–(6), U and P show the water flow's velocity and pressure. Reynolds number (Re) is utilized to describe the behavior of the fluids, and it can be defined as follows [49]:

$$Re=\frac{\rho_{fl}UD_h}{\mu} \tag{7}$$

$$D_h=\frac{4_{Ac}}{P'} \tag{8}$$

In these equations, A_c and P' depict the area of the conduit and wetted perimeter. Nusselt number (Nu) measures the heat transfer capacity in fluid flow systems and is calculated as follows [57]:

$$Nu=\frac{hD_h}{k_{fl}} \tag{9}$$

$$h=\frac{Q}{A_h\left(T_w-T_{fl}\right)} \tag{10}$$

$$Q=q\times A_{hf} \tag{11}$$

The symbol A_h exhibits heat transfer surface area. T_{fl} is the coolant's average temperature inside the microchannel, and T_w is the average temperature of the wall in contact with the coolant. In MCHSs, the pressure drop (ΔP) of the coolant must be evaluated alongside the thermal characteristics of the device. Diodicity (Di) is a phenomenon in which a fluid flows through a system in one direction but is forced to flow in the opposite direction due to the pressure difference between the two ends of the system. It can be formulated by Eq. (12) [58].

$$Di=\frac{\Delta P_r}{\Delta P_f} \tag{12}$$

Understanding and calculating the friction factor (f) and pressure drop are essential for designing and operating efficient fluid transport systems.

$$f = \frac{\Delta P}{\frac{1}{2}\rho v^2} \frac{A_c}{A_{ht}} \tag{13}$$

Examining heat transfer alongside ΔP allows for evaluating the heat sinks' overall performance. The relative efficiency index (REI) displays the total performance of the system, which is expressed as follows [48,59]:

$$REI = \frac{\frac{Nu}{Nu_b}}{\left(\frac{\Delta P}{\Delta P_b}\right)^{1/3}} \tag{13}$$

In the indicator of REI, the Nu and ΔP of each case are evaluated against those of the base case. The subscript of 'b' refers to the base microchannel. There are no types of fins, including dividing fins, curved fins, or triangular-shaped fins, in the base microchannels. According to the REI relation, the influence of the Nu in MCHSs stands out significantly compared to the ΔP. This is due to the relative efficiency index relation in which Nu to power 1 is measured with ΔP to power (1/3). The addition of Tesla valve-shaped fins within the microchannel makes the channel act like a Tesla valve. In this situation, ΔP and following that REI in the forward direction will differ from those in the reverse direction. Therefore, a distinct indicator should be used to compare the REI of the system in forward and reverse directions. The relative efficiency index ratio (REIR) is applied in the present research to show the ratio of the overall performance of the device in the reverse direction to that in the forward direction, as given by Eq. (14) [60].

$$REIR = \frac{REI_r}{REI_f} \tag{14}$$

2.3. Mesh generation and result verification

Mesh generation is an essential part of the numerical process for a variety of issues, such as computational fluid dynamics (CFD), computer-aided design (CAD), and finite element method (FEM). It often requires complex algorithms to create accurate, efficient, and flexible meshes to cover the desired area. In this research, several shapes and sizes of mesh elements were taken into account on the object to generate an accurate mesh. Eventually, considering that the present heat sink includes fins and its geometry is somewhat complex, free tetrahedral elements have been used to cover all points more comprehensively and effectively. Additionally, for uniformity in the mesh, the same mesh elements have been utilized throughout the solid and fluid domains. Fig. 3 depicts the created mesh on the studied microchannel with its Tesla valve-shaped fins. The applied mesh around the fins is refined, which is crucial for accurately capturing the flow and heat transfer phenomena around them. Moreover, finer elements were considered for the fluid domain. To validate mesh independence, several sizes and numbers of elements were adopted in the computational domain. The mesh independency results for Nu and friction factor are presented in Table 2. According to this table, mesh independency was acquired by the element's average size of 28.96 μm^3 (number of elements of 3228462). It can be observed that reducing the element's average size to 17.05 μm^3 does not affect the convergence of the results considerably, while the computational time rises to a large extent. In numeri-

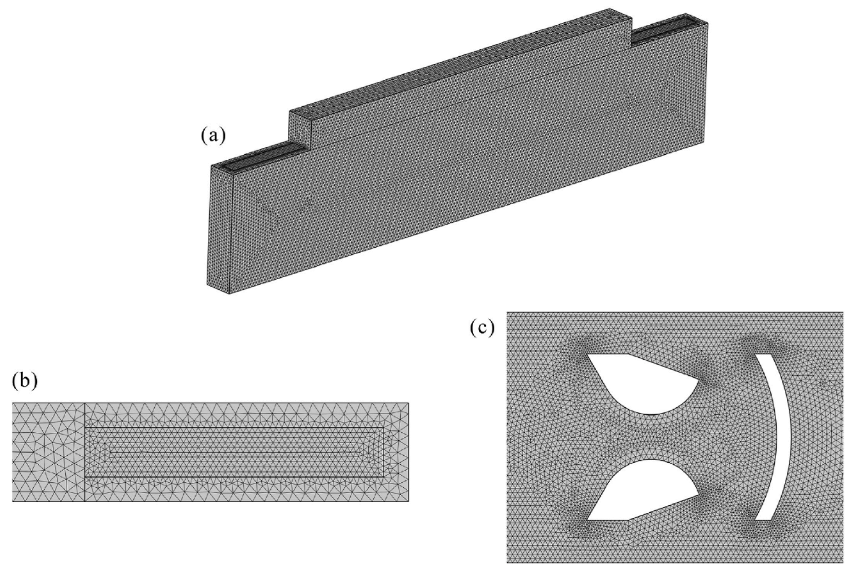

Fig. 3. The created mesh (a) on the studied microchannel, (b) on the top cover and inlet/outlet sections, and (c) near the fins.

Table 2
Mesh independency verification.

Elements average size (μm^3)	Total element numbers	Solve time	Nusselt number		Friction factor	
			Value	Difference (%)	Value	Difference (%)
118.29	790397	00:20:50	15.0411	6.05	0.1156	0.52
65.42	1429192	00:43:38	15.2053	5.02	0.1155	0.60
28.96	3228462	01:38:22	15.7642	1.53	0.1154	0.69
17.05	5485027	03:01:09	16.0099	–	01162	–

cal methods, checking the integrity of the results is necessary because it ensures that the data are accurate and reliable. Tran et al. [52] assessed the thermodynamic behavior of a multi-nozzle MCHS in their numerical work. The model selected to be simulated in this research has the same geometry and boundary conditions specified in their study [52]. Therefore, the data achieved in Ref. [44] verified the current numerical simulation. Total thermal resistance and ΔP findings acquired from the current numerical approach are evaluated with those in the numerical research of Tran et al. [52]. Also, the numerical method utilized in the present work is similar to the technique used to simulate the heat sink presented in the experimental study of Qu et al. [61]. The data of the validation examination are exposed in Fig. 4. According to this figure, an acceptable accord can be seen between the findings of the current investigation and the results of the mentioned references. Therefore, the current simulation is reliable enough to evaluate thermal-hydraulic behavior in the MCHS. After verification examination, some changes are applied to the geometry, and the length of the channels is considered larger. Then, several fins with a Tesla valve shape are embedded within the microchannel to boost heat transfer and provide distinct ΔP values in forward and reverse directions.

2.4. RSM

The RSM is particularly useful in experimental design and optimization processes where the goal is to understand how changes in input variables affect the response. It involves the construction of mathematical models, often polynomial equations, to represent the relationship between the input data and the responses [62]. These models are used to predict the response for different combinations of input variables and to identify optimal conditions for achieving desired outcomes. The second-order equation in RSM is a quadratic polynomial equation that depicts the relationship between the response variable and the input variables. It includes linear, quadratic, and interaction terms to account for the non-linear relationships and interactions between the variables. The general form of a second-order polynomial equation in RSM is [63]:

$$Y = \gamma_0 + \sum_{x=1}^{m} \gamma_x X_x + \sum_{x=1}^{m-1} \sum_{y=x+1}^{m} \gamma_{xy} X_x X_y + \sum_{x=1}^{m} \gamma_{xx} X_x^2 + \varepsilon \tag{15}$$

where γ_0 and ε indicate the fixed coefficient and the statistical error. Besides, X_x and X_y show the input data, while Y displays the response. The orthogonal relationship of parameters in RSM refers to the careful selection and arrangement of experimental runs in a way that ensures the independence of the factors being studied. Orthogonal designs enable the estimation of main effects and interac-

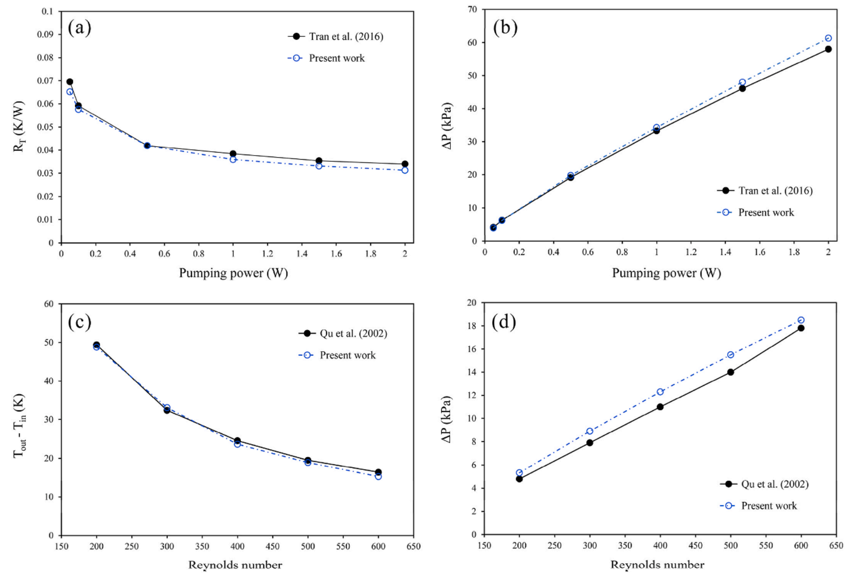

Fig. 4. Model validation through examining the findings of the present investigation and (a) the total thermal resistance data of Ref. [52], (b) the ΔP data of Ref. [52], (c) the difference between outlet and inlet temperatures data of Ref. [61], and the ΔP data of Ref. [61].

tion effects with minimal confounding, allowing for efficient and accurate determination of the factors influencing the response. By employing orthogonal arrays or designs, RSM ensures that the impact of different variables can be assessed independently without interference from other variables. This systematic approach helps researchers identify the most significant factors affecting the response and optimize the process or product accordingly. To provide the orthogonal relation of Eq. (15), the general form can be simplified as follows:

$$Y = \beta_0 + \beta_1 X_1 + \beta_2 X_2 + \beta_{11} X_1^2 + \beta_{22} X_2^2 + \varepsilon \tag{16}$$

2.5. ANN and GA optimization

ANNs are algorithms modeled after the structure and workings of the human brain, used for machine learning and classification tasks. They are composed of interconnected neurons capable of processing data and providing output based on a set of learned parameters [64]. ANNs can be used for many purposes, including image and video retrieval, recommendation systems, robotics, engineering, etc. [65]. The advantages of ANNs include their ability to recognize patterns and correlations in data and make decisions and predictions according to the data they have been trained on [66]. ANNs are also able to generalize and can be used to solve a variety of tasks [67]. Multi-layer perceptron (MLP), as a type of feedforward neural network, is utilized for supervised learning, which means that they are trained with labeled data and can then be used to make predictions on unseen data [68]. The input layer transfers the input data to the next layer until the output layer produces the desired output. This research has applied four ANN models via MATLAB (2016b) software to anticipate the elected responses. Nu and ΔP in each forward and reverse direction are considered as the responses. Table 3 presents the input variables and the levels at which these variables can change. In Table 3, the acute angle of the divider (α), the obtuse angle of the divider (β), and the radius of the divider (R) are selected as the input parameters. To investigate the effects of these parameters comprehensively, three levels of −1, 0, and +1 were chosen. These levels represent different values within the range of each parameter: level −1 represents the lowest value of the input parameters, level 0 is the midpoint value, and level +1 denotes the maximum value of the input parameters, representing the upper limit of the design constraints. The selection of these levels ensures a thorough examination of the impact of changing each input parameter on the performance of the MCHS. Besides, the ranges are chosen according to the geometrical limitations of the MCHS and the Tesla valve-shaped fins. For instance, the minimum value (−1 level) for α is determined by the smallest angle that still allows efficient fluid flow without causing excessive pressure drops. The midpoint (0 level) is selected as a balanced angle that optimizes flow while maintaining structural integrity. The maximum value (+1 level) represents the largest feasible angle before the design becomes impractical due to space constraints within the MCHS. The structure of the ANN models is as follows.

- An MLP of 3-6-1 for predicting the Nu in the forward direction (Nu_f).
- An MLP of 3-6-1 for predicting the Nu in the reverse direction (Nu_r).
- An MLP of 3-6-1 for predicting the ΔP in the forward direction (ΔP_f).
- An MLP of 3-5-1 for predicting the ΔP in the reverse direction (ΔP_r).

In the abovementioned ANN models, the number of neurons in the input (3), hidden (6), and output (1) layers are identical for all models, and only the neuron number in the hidden layer of the ANN for predicting the ΔP_r is different. In an ANN, the amount of neurons in a hidden layer is designated by the complexity of the issue that the ANN is attempting to address. Different architectures were experimented with to find the best models when designing ANN models. Through testing, it was determined that with the neuron numbers 6, 6, 6, and 5 for the ANN models of Nu_f, Nu_r, ΔP_f, and ΔP_r, respectively, the network provides appropriate accuracy in predicting the responses. With the neuron numbers higher than the mentioned values, the overfitting problem happens. On the other hand, the iterations of the ANN to acquire the desired output increase to a large extent, resulting in a slow data convergence. Fig. 5a and b illustrate the topology of the ANNs and the operations performed in the neurons, respectively. The current study employs the full factorial method to determine the number of tests. This design comprehensively evaluates the effects of all variables and their interactions on the responses. If k variables are present, each having m levels, a full factorial design recommends to have m^k experiments. In the current research, the three input variables, each at three levels, yields a total of 27 experimental runs. In this design, all of the three variables are set at three levels of +1, 0, and −1 (Table 3). Given the time-consuming and costly nature of experimental and numerical works, efforts are made to minimize the number of tests. The full factorial method is employed to select tests that significantly impact the responses. Hence, this study has been utilized to identify sensitive and effective scenarios and conduct tests accordingly. The dataset is divided into training, validation, and testing sets, comprising 70 %, 15 %, and 15 % of the total data, respectively. Training data are used to teach a machine learning model to recognize patterns and make predictions based on input features. They serve as the foundation for the model's learning process, where it adjusts its internal parameters to minimize errors in predicting the output. Unlike training data, validation data are not used to update the model's parameters. Test data are held out from the model

Table 3
Input variables and the levels at which these variables can change.

Variable parameter	Label of normalized form	Levels of variable		
		−1	0	+1
α (degree)	A	30	45	60
β (degree)	B	140	160	180
R (μm)	C	40	60	80

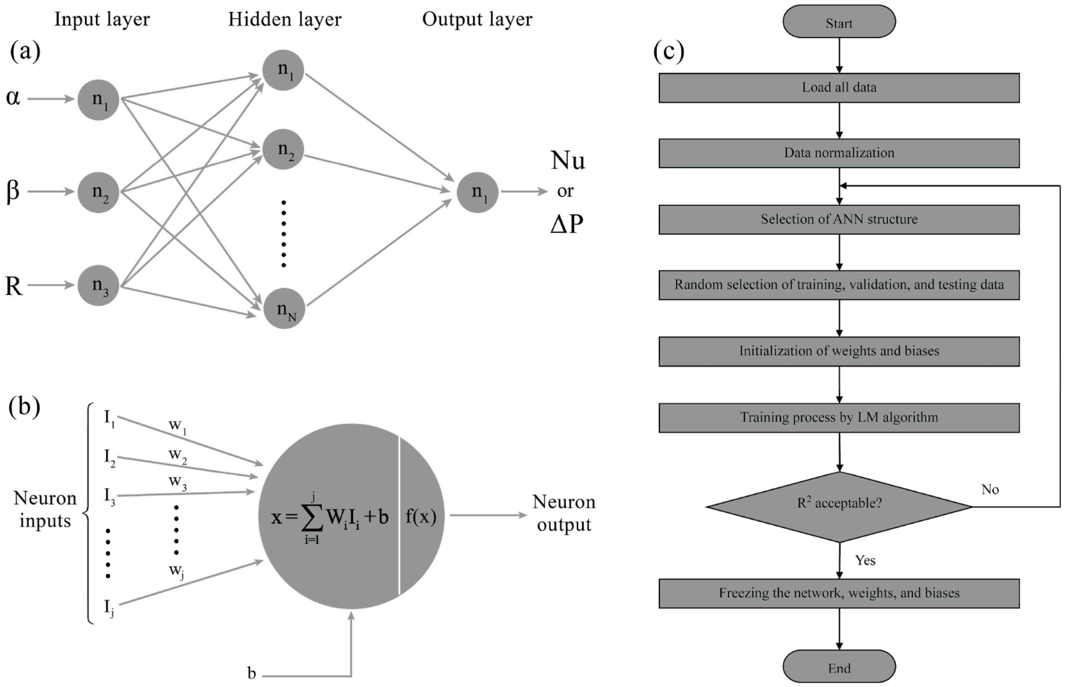

Fig. 5. (a) general topology of the ANNs, (b) the operations performed on neurons, and (c) the flowchart of the ANNs.

during training and validation. The list of the 27 tests with the values of input variables for each test is presented in Table 4. In this research, the Levenberg-Marquardt algorithm trains the applied networks. Weights and biases are critical components in offering the prediction models. They are vital in determining the behavior of the network during the training. Besides, the hyperbolic tangent function is regarded for the applied models hidden layer. While for the output layer, the linear function is exerted. Fig. 5c depicts the

Table 4
The selected 27 combinations of variables for the study.

Test	Variables		
	α (degree)	β (degree)	R (μm)
1	45	180	80
2	45	180	40
3	60	160	80
4	60	180	40
5	30	140	60
6	30	180	80
7	45	160	40
8	45	160	60
9	30	180	60
10	45	180	60
11	30	160	80
12	45	140	60
13	30	160	60
14	45	140	40
15	60	160	40
16	60	180	60
17	30	180	40
18	30	160	40
19	45	160	80
20	60	160	60
21	60	140	60
22	60	180	80
23	60	140	80
24	60	140	40
25	30	140	40
26	30	140	80
27	45	140	80

flow chart of the applied ANNs. Single-optimization methods face accuracy challenges as they provide just one optimized design point within the entire space. In contrast, multi-objective optimization approaches yield a collection of Pareto-optimal solutions, encompassing minimized or maximized responses while adhering to design constraints. Of the optimization techniques introduced thus far, the GA stands out as the latest and most practical choice, surpassing other methods due to its capacity to effectively optimize complex, non-differentiable, implicit, and multi-objective challenges. In the current GA optimization, the number of generations and populations were 300 and 200, respectively. These numbers of population and generation are selected according to the number of input variables in the models. Cost functions are a measure of error used in ANNs to estimate how successfully models perform. They measure the discrepancy between the anticipated and actual values. The determination coefficient (R^2), the mean absolute error (MAE), and the root mean squared error (RMSE) are the main cost functions utilized to evaluate the present ANN models.

$$R^2 = 1 - \frac{\sum_{i=1}^{m} \left(r_{num} - r_{pred}\right)^2}{\sum_{i=1}^{m} \left(r_{num} - \overline{r_{num}}\right)^2} \tag{17}$$

$$MAE = \frac{1}{m} \sum_{i=1}^{m} \left| r_{pred} - r_{num} \right| \tag{18}$$

$$RMSE = \sqrt{\frac{1}{m} \sum_{i=1}^{m} \left(r_{pred} - r_{num}\right)^2} \tag{19}$$

3. Results and discussion

3.1. Results of the current simulation

This work aims to use fins with special shapes inside the investigated multi-nozzle MCHS, which can eventually make the microchannels act like a Tesla valve. In Tesla valves, there is a difference between the flow characteristics in forward and reverse directions. Therefore, it should be distinguished between the heat transfer, pressure drop, and relative efficiency index of the device when the flow direction switches. Table 5 lists the Nu_f, Nu_r, ΔP_f, ΔP_r, REI_f, and REI_r values of the device resulting from numerical simulation for every test. This table also contains the relative efficiency index ratio and the diodicity values to indicate how the total performance and pressure drop have changed as the flow direction alters. It is noticed that the geometric factors of the divider, such as the

Table 5
Results achieved from numerical simulation.

Test number	Numerical outcomes							
	Nu_f	Nu_r	ΔP_f (kPa)	ΔP_r (kPa)	REI_f	REI_r	REIR	*Di*
1	36.596	45.949	145.700	222.000	1.355	1.478	1.091	1.524
2	35.288	42.564	140.000	202.000	1.324	1.413	1.067	1.443
3	37.951	46.385	150.250	207.000	1.391	1.528	1.098	1.378
4	37.459	45.196	143.420	211.610	1.394	1.478	1.060	1.475
5	34.822	38.401	142.300	192.160	1.299	1.297	0.998	1.350
6	34.245	40.752	138.700	202.900	1.289	1.351	1.048	1.463
7	34.962	40.846	141.010	201.440	1.309	1.358	1.037	1.429
8	35.783	42.865	145.540	209.800	1.325	1.405	1.060	1.442
9	33.783	38.931	135.600	193.510	1.281	1.311	1.024	1.427
10	35.889	43.444	141.700	210.100	1.341	1.424	1.062	1.483
11	34.598	39.637	142.830	199.150	1.290	1.322	1.025	1.394
12	37.046	42.393	153.040	209.820	1.349	1.390	1.030	1.371
13	34.705	38.634	141.200	192.530	1.298	1.304	1.004	1.364
14	36.176	41.240	148.800	201.610	1.330	1.370	1.030	1.355
15	36.425	44.649	142.200	210.840	1.360	1.462	1.075	1.483
16	37.361	47.016	143.670	213.300	1.390	1.533	1.103	1.485
17	33.920	38.003	134.130	187.180	1.291	1.294	1.003	1.396
18	34.249	38.054	138.060	187.550	1.291	1.295	1.003	1.358
19	36.355	44.653	148.350	217.350	1.338	1.447	1.081	1.465
20	37.478	46.742	146.530	212.320	1.385	1.527	1.102	1.449
21	37.629	45.991	150.350	213.010	1.379	1.500	1.088	1.417
22	38.453	48.066	152.800	211.700	1.401	1.571	1.121	1.385
23	38.654	47.000	163.460	208.900	1.377	1.543	1.120	1.278
24	37.001	45.045	145.550	211.720	1.370	1.472	1.074	1.455
25	34.898	37.779	140.510	187.400	1.308	1.286	0.983	1.334
26	35.362	38.699	144.020	196.570	1.314	1.297	0.987	1.365
27	37.985	44.111	157.980	217.580	1.369	1.429	1.044	1.377

acute angle, the obtuse angle, and its radius affect the Nu, ΔP, and REI of the heat sink in both forward and reverse directions. Nonetheless, the main effect of these factors is when the flow direction is shifted to reverse. To ensure optimal functioning of the device, it is imperative to enhance heat transfer and decrease pressure drop. The highest Nu_f and Nu_r occur in the configurations of tests number 23 and 22, respectively. Moreover, when the configurations of test number 17 are exerted in manufacturing the channels of the heat sink, the minimum values of pressure drop in both directions are acquired, respectively. It is realized that the pressure drop is higher when the coolant moves in the reverse direction since the Tesla valve-shaped fins are designed to minimize the risk of backflow. REI_r denotes the total performance of the device when the direction is reversed. At the same time, REI_f indicates it when the flow direction is forward. In test number 22, the maximum REI_f and REI_r are recorded at 1.401 and 1.571, respectively. Considering REIR values, if it is greater than 1, it means that the system's total performance in reverse mode is higher than its performance in forward mode. Test number 22 has the highest value of REIR, which indicates that in the MCHS with the configurations of test number 22, the total performance of the device in the reverse direction is about 12.1 % higher than that of the forward direction. Besides, test number 1 has the highest diodicity value, whish represents that the ΔP_r is increased by about 52.4 % compared to that of the forward direction.

Fig. 6 illustrates the image of resultant temperature and pressure contours for forward and reverse flows. Tests 4, 6, 22, and 23 are considered to be investigated these contours. The selection of these tests was based on their strategic importance in understanding the impact of each parameter on the performance of the system. Test number 22 is considered the base case in the analysis, where all parameters (α, β, and R) are set at their maximum values (level +1). This configuration serves as a reference point against which other tests are compared. In each of the other selected tests (4, 6, and 23), all parameters are kept constant at their level +1 values, except for one parameter, which is changed from level +1 to level −1. This approach allows to isolate and investigate the effect of the maximum change of each parameter on the system's behavior. For instance, test 23 focuses on the parameter β. Here, all parameters are set to level +1 like in the base case (test 22), but β is altered from level +1 to level −1. This test depicts the role of changing β on the system's performance. While, tests number 4 and 6 examine the impact of R and α, respectively. Fig. 6a and b depict the temperature distribution across the microchannel and around the fins, which can provide insights into the thermal features of the channel. In all configurations of microchannels, the maximum temperature occurs at the outlet section and on the bottom surface of the heat sink. The temperature distribution shows a gradient from the high-temperature regions near the heat source to the cooler regions away from it. This indicates that the heat transfer is more localized, with higher temperatures near the source. In the reverse direction, the temperature distribution is different. The maximum temperature observed is relatively lower than that of the forward direction. This suggests that there is higher heat transfer efficiency in the reverse direction. It is noticeably visible that in the reverse direction, the temperature distribution in the device's substrate (solid domain) is better and more uniform. This is attributed to the generation of more vortices in the fluid flow in this direction. These vortices enhance the mixing of the fluid, leading to more contact with the heat transfer surfaces and thereby increasing the overall heat transfer rate. However, in the forward direction, the flow is more streamlined with fewer disturbances, resulting in higher localized temperatures on the bottom surface of the heat sink. The lack of sufficient mixing reduces the overall heat transfer efficiency. The rise in temperature can diminish electronic equipment's stability, and a lower solid temperature means efficient heat dissipation performance in practical applications. Thus, in the investigated MCHS with fins in the shape of a Tesla valve, it is easy to prevent the temperature rise in the solid part of the MCHS by switching the flow direction. Pressure contours in a microchannel are used to visualize the channel's pressure distribution. They can help identify areas of high pressure drop and indicate potential areas for optimization. The pressure contours in the forward direction display a relatively uniform distribution with lower pressure gradients. The pressure required to maintain fluid flow in the forward direction is significantly lower, as indicated by the smoother and more consistent pressure distribution. The fluid flows more freely in this direction, encountering fewer obstacles and generating fewer vortices. Conversely, the pressure contours in the reverse direction show higher pressure gradients and more complex patterns. The pressure required to drive the fluid flow in the reverse direction is much higher than in the forward direction. Hence, the inlet and outlet pressure difference is higher in the reverse direction. One primary reason for this increased pressure requirement is the generation of more vortices in the fluid flow. The other reason is the shape of the fins, so that when fluid flows in the reverse direction, it hits the fins. The fins obstruct the straightforward path of the fluid, causing it to navigate around these structures. This obstruction hinders simple flow, leading to increased pressure drop and higher pressure gradients required to maintain flow. As can be seen in the figure, test 6 has the lowest pressure drop in both directions among the investigated tests. The reason for this is the shape of the dividers, the dividers with a lower height prevent the movement of the fluid, and on the other hand, less friction is created. Test 23, however, has the highest pressure drop in the forward direction because in this test, the dividers are placed as obstacles in the flow direction and create more vortices.

Fig. 7 depicts the velocity and streamline distributions in different configurations of the microchannels. As observed in velocity contours, the highest velocity created in reverse flow is more remarkable than that in forward flow. The reason is the geometry of the fins applied inside the microchannels, which causes distinct ΔP in both forward and reverse directions. According to Bernoulli's principle, as the fluid flow passes through the fins, more ΔP occurs in the reverse direction, which raises the water velocity. It is deduced that the applied fins, inspired by the Tesla valves' structure, perform properly and create pressure diodicity (the main aim of Tesla valves). Besides, the fluid is more in contact with the different parts of the fins, and due to successive collisions, more intense vortices are created and cause a better heat transfer in reverse flow. The advantage of using this design is that under different circumstances, depending on whether more heat transfer is required or less ΔP, the flow direction can be changed, and the maximum possible performance of the device can be accessed.

To provide information about the direction and velocity of the fluid within the microchannels, the streamlines of these channels are represented in Fig. 7b. According to this figure, it can be understood how changes in the shape and size of Tesla valve-shaped fins affect the fluid flow. Besides, by examining the density of the streamlines in microchannels with the forward flow, it can be observed

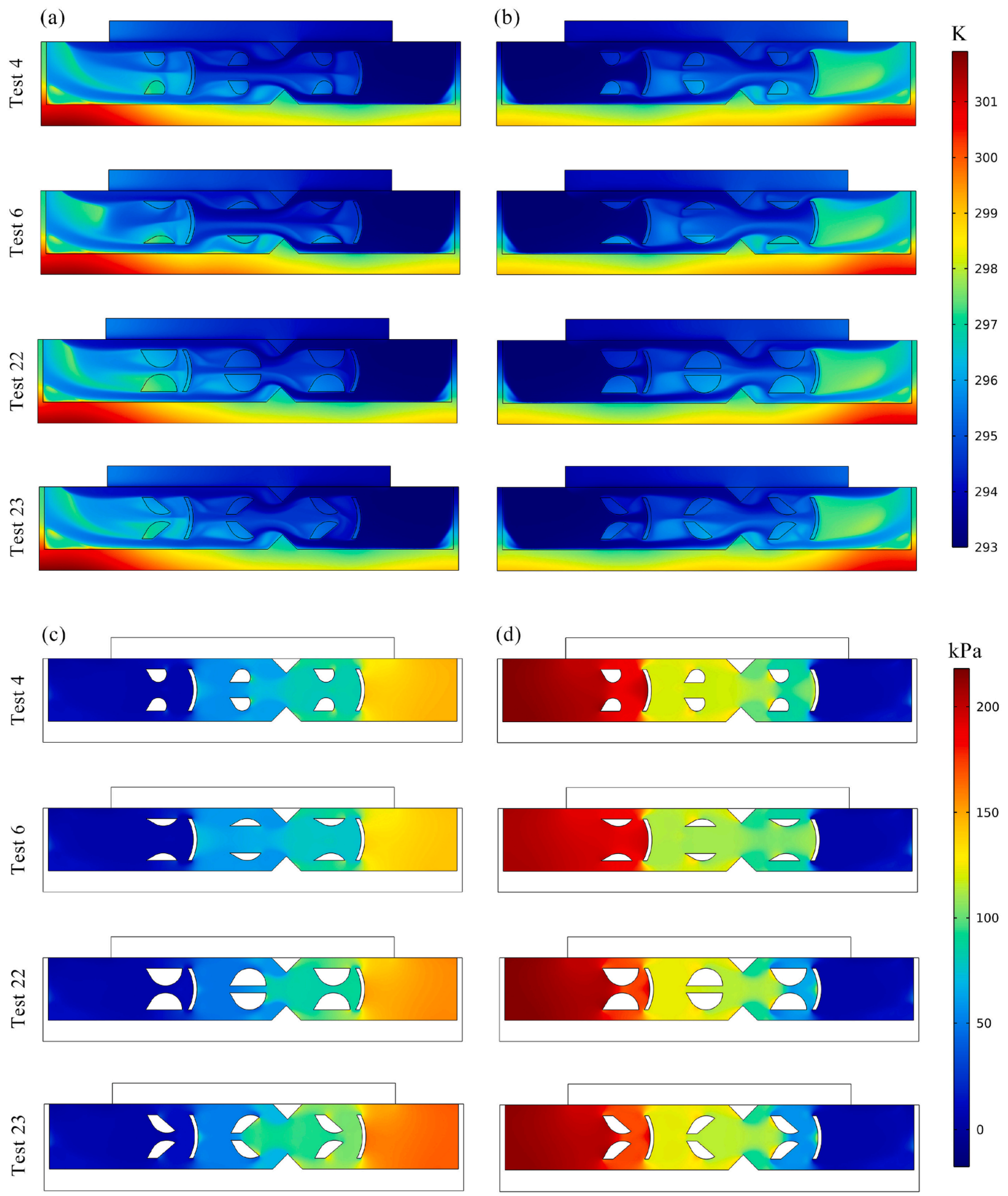

Fig. 6. Temperature contours are depicted for (a) the forward and (b) the reverse direction across various microchannel configurations. Pressure contours are illustrated for (c) the forward and (d) the reverse direction across multiple microchannel configurations.

that because of the structure of the fins, most of the flow tends to pass near the channels' walls and between the second column fins. Thus, less fluid mixing, fewer vortices, and less ΔP occur against the forward flow. In all tests, it is evident that vortices are generated downstream of the obstacles. This occurs because the flow separation happens as the fluid encounters the obstacles, leading to the formation of low-pressure regions and subsequently vortices in the wake of these obstacles. When fluid flows in the reverse direction, vortices are generated upstream of the concave obstacles. These vortices form between the obstacles and the dividers due to the interaction of the fluid with the curved surfaces, causing the flow to separate and roll into vortices. The density of the streamlines provides insights into the flow intensity and mixing. Higher density indicates stronger and more numerous vortices. It can be observed that the intensity and number of vortices are higher when the flow is in the reverse direction, indicating enhanced mixing and more complex flow structures. In test 6, when the fluid flows in the reverse direction and encounters the concave fins, it is noted that such vortices are not significantly formed upstream. The fluid passes through the channel more smoothly, suggesting less obstruction and easier passage of the fluid. In contrast, test 23 exhibits different behavior due to the presence of a β. This angle creates a region between the dividers and the concave fins where more vortices are produced. This enhanced vortex formation improves mixing and heat transfer,

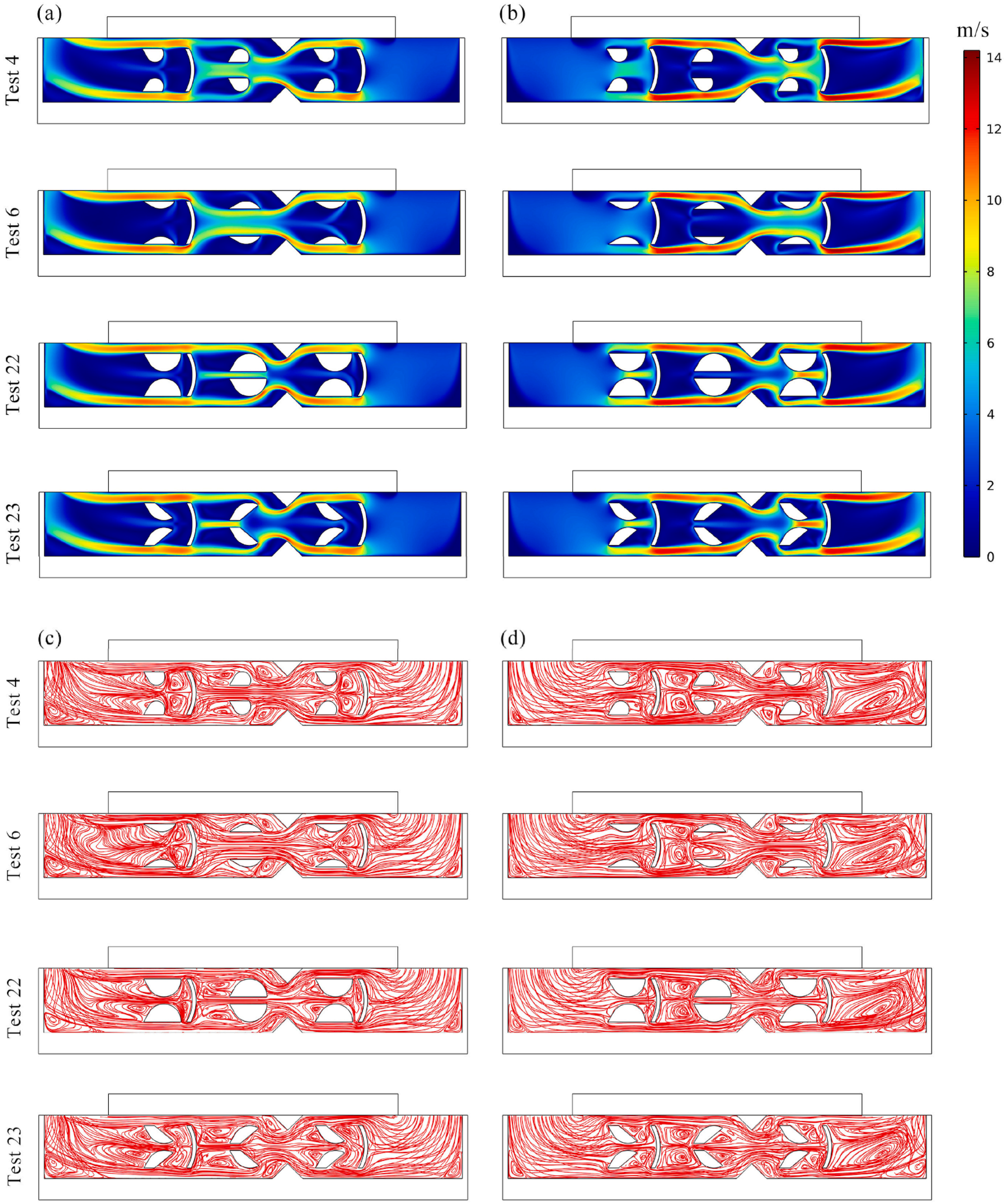

Fig. 7. Velocity contours are shown for (a) the forward and (b) the reverse direction across different microchannel configurations. Streamlines are displayed for (c) the forward and (d) the reverse direction across various microchannel configurations.

as the fluid experiences more vigorous turbulence and interaction with the channel walls. The vortices observed in the streamline contours are actually wakes generated in the downstream region of the fins. They are somewhat low-pressure layers that create a rotational flow to facilitate easier heat transfer. They do not lead to the formation of turbulent flow; rather, the flow remains laminar and moves smoothly over these layers.

3.2. Results of RSM and ANN models

As previously discussed, one of the primary uses of ANNs is to predict responses. At first, the ANN models used to indicate the responses of the present paper are trained utilizing the Levenberg-Marquardt algorithm. To avoid repeating each model in the paper, a generalized expression of these ANN models is defined via Eqs. (18) and (19). As it is clear from the general form of these equations, ANN models need several weights and biases to forecast the Nu and ΔP. After examining various weights and biases, the best amounts of them for the four ANN models are identified. Tables 6–9 represent the obtained weights and biases for ANNs of Nu_f, Nu_r, ΔP_f, and ΔP_r, respectively. Then, the response values, which have been achieved from the simulation before, are anticipated through the ANN

Table 6
Obtained data for the network of Nu_f.

Hidden layer				Output layer	
Weights (6 × 3)			Biases (6 × 1)	Weights (1 × 6)	Biases (1 × 1)
−1.4783	2.3096	1.4157	−2.2255	0.1390	−0.1096
−0.8091	−1.0930	−0.1381	−0.8178	0.7942	
−0.0258	−1.7401	−1.9274	−1.6195	−0.2678	
−0.5216	0.0225	−0.1660	−0.1378	−1.9840	
−0.4137	0.5899	−2.3023	−2.4033	0.2522	
2.4067	1.2415	−1.6295	3.7075	0.3461	

Table 7
Obtained data for the network of Nu_r.

Hidden layer				Output layer	
Weights (6 × 3)			Biases (6 × 1)	Weights (1 × 6)	Biases (1 × 1)
0.2931	1.8355	1.1683	−3.8271	0.5371	0.3685
−3.9390	0.5716	−2.8697	2.5401	−0.1014	
−0.6226	−1.8643	1.8419	0.9069	0.0614	
−1.2870	−0.2174	−0.3221	−0.3674	−0.8185	
−1.9528	0.5478	0.0319	−2.0822	0.0221	
−1.4281	2.4295	1.0035	−2.6062	−0.0029	

Table 8
Obtained data for the network of ΔP_f.

Hidden layer				Output layer	
Weights (6 × 3)			Biases (6 × 1)	Weights (1 × 6)	Biases (1 × 1)
0.4829	0.4630	2.2526	−3.4638	0.7116	−0.1936
−2.3187	−1.9955	−2.5569	1.7946	0.0013	
0.5596	1.9319	−0.4784	1.8532	−1.2169	
−0.3368	−2.7654	−2.1565	−1.3081	−0.1701	
0.6648	−1.2671	0.2293	1.6695	0.5224	
1.3306	1.7296	−0.4886	2.4145	1.2326	

Table 9
Obtained data for the network of ΔP_r.

Hidden layer				Output layer	
Weights (5 × 3)			Biases (5 × 1)	Weights (1 × 5)	Biases (1 × 1)
0.1965	−2.3532	−2.4903	3.2241	−0.1839	−0.2552
1.6505	2.5209	−2.9174	2.8224	0.0182	
0.4695	0.0140	−0.7048	0.2446	−0.3979	
1.8106	0.3799	2.3901	−3.5961	−0.4035	
−2.2413	0.0154	−0.4065	−0.5766	−0.7897	

models to be compared with the available values. Fig. 8a - d evaluates the values acquired via the numerical approach and those forecasted through the ANNs. Based on these figures, the outcomes of both approaches are adjacent. It is evident from the comparison of the outputs that the ANN models successfully accurately predict the responses.

$$\begin{bmatrix} a_1 \\ a_2 \\ . \\ a_N \end{bmatrix} = Weights_{HL} \times \begin{bmatrix} 2 \times \dfrac{\alpha - min(\alpha)}{max(\alpha) - min(\alpha)} - 1 \\ 2 \times \dfrac{\beta - min(\beta)}{max(\beta) - min(\beta)} - 1 \\ 2 \times \dfrac{R - min(R)}{max(R) - min(R)} - 1 \end{bmatrix} + Biases_{HL} \tag{18}$$

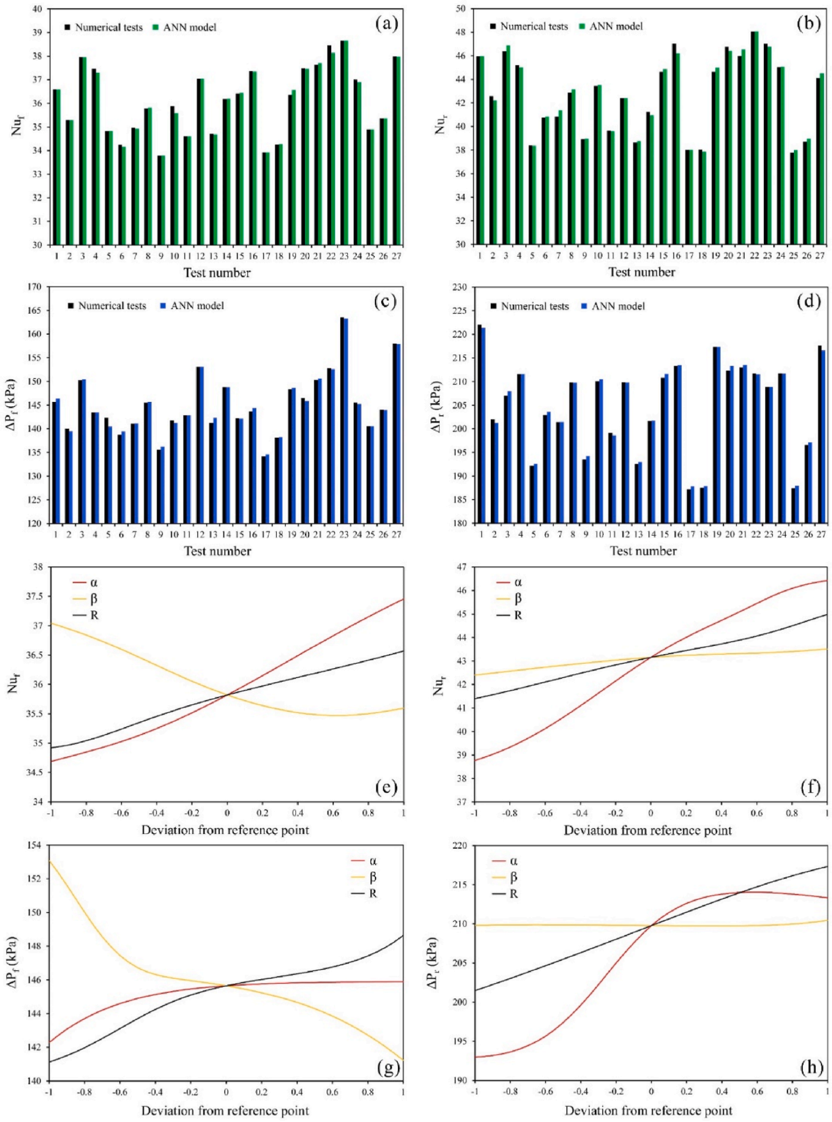

Fig. 8. Comparison between the (a) Nu_f, (b) Nu_r, (c) ΔP_f, and (d) ΔP_r values achieved from the numerical approach and those anticipated via the ANNs. Perturbation diagrams indicating the impact of each variable's variation on (e) Nu_f, (f) Nu_r, (g) ΔP_f, and (h) ΔP_r.

$$Response = \left(Weights_{OL} \times \begin{bmatrix} \frac{2}{1 + exp\left(-2a_1\right)} - 1 \\ \frac{2}{1 + exp\left(-2a_2\right)} - 1 \\ \vdots \\ \frac{2}{1 + exp\left(-2a_N\right)} - 1 \end{bmatrix} + Bias_{OL} + 1 \right) \times \frac{max\,(Target) - min\,(Target)}{2} + min\,(Target) \tag{19}$$

Tables 10–13 exhibit the analysis of variance of the neural networks for all responses. The p-value, short for "probability value," is a measure used in statistical hypothesis testing to determine the strength of evidence against the null hypothesis. In simpler terms, it tells us the probability of obtaining the observed results (or results more extreme) if the null hypothesis were true. A small p-value (typically less than a predefined significance level, often denoted α, such as 0.05) indicates strong evidence against the null hypothesis. The p-value alone does not provide information about the practical significance or the size of the effect; it only indicates whether the effect is statistically significant or not. The F-value is a statistic used to determine whether the means of three or more groups are significantly different from each other. Analysis of variance works by comparing the variance between group means to the variance within groups. The F-value is calculated by dividing the between-group variance by the within-group variance. If the F-value is suffi-

Table 10
The analysis of variance for Nu_f.

Source	Sum of square	Mean square	F-value	P-value
Model	54.606	18.202	1457.249	< 0.001
A	34.833	34.833	2788.781	< 0.001
B	10.920	10.920	874.247	< 0.001
C	12.245	12.245	980.327	< 0.001
Residual	0.287	0.012		

Table 11
The analysis of variance for Nu_r.

Source	Sum of square	Mean square	F-value	P-value
Model	286.768	95.589	892.724	< 0.001
A	265.833	265.833	2482.649	< 0.001
B	5.881	5.881	54.925	< 0.001
C	57.824	57.824	540.024	< 0.001
Residual	2.463	0.107		

Table 12
The analysis of variance for ΔP_f.

Source	Sum of square	Mean square	F-value	P-value
Model	1103.163	367.721	1058.566	< 0.001
A	73.325	73.325	211.082	< 0.001
B	645.587	645.587	1858.466	< 0.001
C	258.488	258.488	744.114	< 0.001
Residual	7.990	0.347		

Table 13
The analysis of variance for ΔP_r.

Source	Sum of square	Mean square	F-value	P-value
Model	2482.312	827.437	2485.557	< 0.001
A	2123.653	2123.653	6379.286	< 0.001
B	2.768	2.768	8.315	0.008
C	1132.119	1132.119	3400.796	< 0.001
Residual	7.657	0.333		

ciently large, it suggests that the variance between group means is larger than the variance within groups, indicating that there is likely a significant difference between at least one pair of group means. Here, the higher F-values and lower p-values indicate the validity of the ANN models based on the observed data. The best orthogonal relation for all responses, which have been derived via the RSM, are displayed as follows:

$$Nu_f = 35.892 + 1.546 \times A - 0.365 \times B + 0.545 \times C - 0.176 \times A^2 + 0.420 \times B^2 + 0.088 \times C^2 \tag{20}$$

$$Nu_r = 42.917 + 3.733 \times A + 0.515 \times B + 1.215 \times C - 0.620 \times A^2 + 0.314 \times B^2 - 0.012 \times C^2 \tag{21}$$

$$\Delta P_f = 145.136 + 4.493 \times A - 3.905 \times B + 3.912 \times C - 2.703 \times A^2 + 1.655 \times B^2 + 0.995 \times C^2 \tag{22}$$

$$\Delta P_r = 209.874 + 8.969 \times A + 0.863 \times B + 4.544 \times C - 8.003 \times A^2 + 0.951 \times B^2 - 0.478 \times C^2 \tag{23}$$

Perturbation plots have been used to analyze the influence of the input data on the outputs of four ANN models. They show the change in the outputs of the models when the values of a single input variable are changed within its coded levels while all other input variables remain constant. This allows to identify which input variables are most important in influencing the model's output. Fig. 8e - h depict the perturbation plots for Nu_f, Nu_r, ΔP_f, and ΔP_r. The variable with the steepest incline is the most influential in all these plots. Based on these figures, in microchannels with the forward flow, the acute angle of the divider and the obtuse angle of the divider have the most considerable role in the Nu and ΔP, respectively. In contrast, when the flow direction changes, the acute angle of the divider becomes the parameter with the greatest impact on the Nu and ΔP. Increasing the parameter of α increases both the Nu_f and Nu_r. The reason is the higher heat transfer surface area that is created by higher acute angles. At the same time, more vortices with larger sizes are created, which causes more fluid mixing and, ultimately, more heat transfer. Conversely, at lower values of α, the majority of the fluid's flow rate passes through the middle dividers in the device with the forward flow and causes the fluid to have less contact with the channel walls. Naturally, poor heat transfer and pressure drop occur. At higher values of α, however, the fluid spreads in all parts around the dividers and causes more heat transfer and ΔP. By raising the parameter of R, a behavior similar to that caused by larger acute angles is observed. In a heat sink with forward flow, the Nusselt number increases with decreasing β because the angle created at the lower surface of the dividers provides enough space for fluid to enter this area. Thus, the vortices in this area cause more heat transfer. At higher values of β, more fluid passes through the sides of the channel, causing it to experience less pressure drop. While in lower values of β, the majority of the coolant passes through the center of the microchannel and between the fins, experiencing a higher pressure drop. When the movement direction is reversed, the fluid is directed by the dividers to the center of the microchannel and experiences more heat transfer than the forward mode. Since the heat transfer surface is greater in larger fins, more heat transfer occurs, even though larger fins obstruct the flow more. The effect of β on ΔP_r is less than the other parameters because the main passages available for fluid flow do not change remarkably with the change of β, and as a result, the pressure drop changes are small. With the decrease of α and R, the side passages and the space between the dividers increase, which causes a noticeable diminish in pressure drop.

When the acute angle of the divider rises from its minimum level to the maximum one in Fig. 8e, Nu_f enhances. On the other hand, as the obtuse angle of the divider rises, Nu_f reduces. Considering the perturbation plots for ΔP_f, with the same assumptions, it is realized from Fig. 8g that pressure drop is also increased, while with the increase in β, pressure drop in the microchannels with forward flow decreases. From the perturbation plots of reverse flow (Fig. 8f), an increment in Nu_r is obtained when α and β increase from their minimum to maximum level, respectively. Regarding the pressure drop plots in the reverse direction, an improvement in ΔP_r is achieved when α and β rise (Fig. 8h). It is easily observable that with an increase in the radius of the divider, each of the four responses enhances noticeably. In the multi-nozzle MCHS with a higher acute angle of the divider, depending on whether more heat transfer is needed or less pressure drop, the flow direction can be changed, and the desired demand can be acquired.

The three-dimensional surface plots for Nu and ΔP are represented in Fig. 9. They display the relation between the three parameters of α, β, and R. As α increases, the Nusselt number in forward flow is enhanced. This increment is more noticeable at greater values of β (Fig. 9a) and R (Fig. 9b). Moreover, an increase in R raises Nu_f, and its effect is more noticeable in lower β values (Fig. 9c). It is

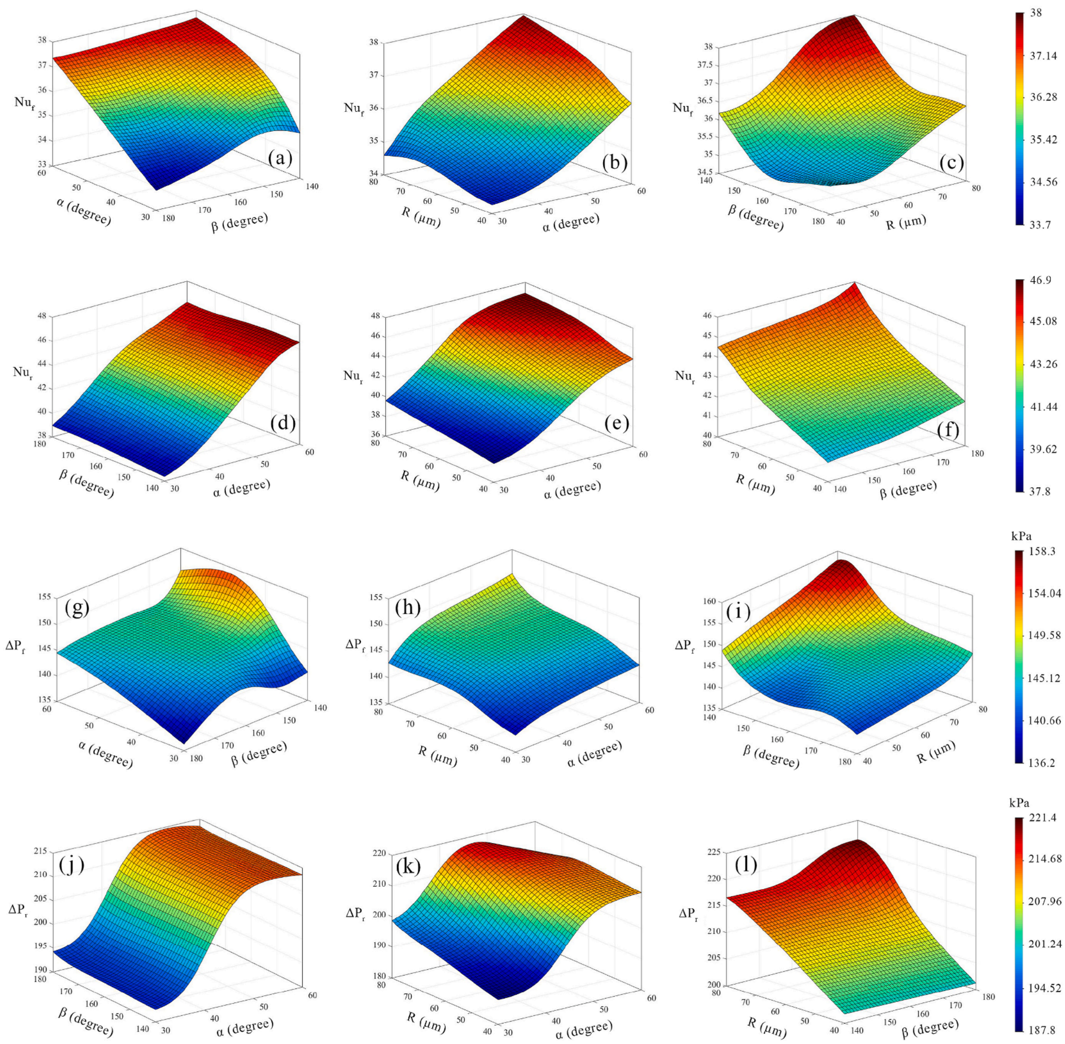

Fig. 9. 3D contours of all responses.

found out from Fig. 9d - f that the variable of α owns a notable role in the Nu_r. All of the contents mentioned related to the three-dimensional contours were affirmed via the perturbation plots before. Considering the pressure drop plots, with an increase in α, ΔP_f enhances (Fig. 9g). The role of the variations of α in ΔP_f is more considerable at lower values of β. Enhancing the parameter of R increases the ΔP_f (Fig. 9h and i). Taking the reverse flow contours into account, the variable of α has the greater impact on the ΔP_r compared to the parameter of β (Fig. 9j). The impact of α on the ΔP_r is the same at both higher and lower values of β. Besides shifting the parameter of α, the alteration of R affects the ΔP of the coolant in the channels with a reverse direction to an extent (Fig. 9k and l). The influence of R on the ΔP of the system in the reverse direction is more considerable at greater values of β. The perturbation diagrams obtained from the RSM were similar to the perturbation diagrams of the ANN models, indicating that both accurately predicted the impact of structural parameters on the responses.

3.3. Optimization results

As previously discussed, the simulation data is employed as the benchmark for training the ANN models. Then, the predicted results by the ANN models are compared with these data. Cost functions help to evaluate how well the ANN and RSM models are performing in terms of their ability to predict the responses correctly. Table 14 discloses the cost function data for assessing the accuracy of ANN and RSM models. Based on this table, all of the ANN and RSM models with R^2 values close to 1 indicated a perfect fit. Conversely, the ANN and RSM models should have lower MAE and RMSE values to be appropriate enough to produce the best results. Table 14 shows that the ANN and RSM models exhibiting MAE and RMSE values that approach zero perform well in predicting Nu_f, Nu_r, ΔP_f, and ΔP_r. By comparing the outcomes between the RSM and ANN models, it is noticed that the accuracy of the ANN model is slightly higher than that of the RSM model. Thus, here, all anticipations have been made exerting the ANN model. Tables 15 and 16 demonstrate the RMSE values and independence of data from the number of neurons. To enhance the precision of predictive models, the present study initiates with a small number of neurons, minimizing the risk of overfitting. Tables are displayed starting from 2 neurons onwards, as a single neuron was unable to anticipate the responses. The number of neurons in the hidden layer is gradually rised to explore the point at which overfitting starts. Based on Tables 15 and in the end, six neurons have been chosen for the ANN

Table 14
Cost functions for assessing the ANN and RSM model's accuracy.

Cost function	ANN				RSM			
	Nu_f	Nu_r	ΔP_f	ΔP_r	Nu_f	Nu_r	ΔP_f	ΔP_r
R^2	0.995	0.992	0.993	0.997	0.934	0.980	0.870	0.865
MAE	0.055	0.228	0.367	0.425	0.303	0.361	1.836	2.854
RMSE	0.103	0.302	0.544	0.533	0.369	0.470	2.326	3.590

Table 15
Selecting the number of neurons for the hidden layer of the Nu models.

Number of neurons in the hidden layer	RMSE							
	Prediction model of Nu_f				Prediction model of Nu_r			
	Train data	Validation data	Test data	Epoch	Train data	Validation data	Test data	Epoch
2	1.556	2.841	3.204	40	1.025	2.999	3.210	38
3	0.802	1.100	1.856	35	0.806	2.267	2.350	37
4	0.352	0.509	0.661	38	0.554	1.670	1.697	30
5	0.123	0.331	0.421	32	0.388	0.901	0.991	27
6	0.080	0.214	0.293	29	0.301	0.737	0.708	23
7	0.051	0.261	0.279	25	0.288	0.747	0.701	22
8	0.022	0.389	0.426	23	0.201	0.836	0.845	22

Table 16
Selecting the number of neurons for the hidden layer of the ΔP models.

Number of neurons in the hidden layer	RMSE							
	Prediction model of ΔP_f				Prediction model of ΔP_r			
	Train data	Validation data	Test data	Epoch	Train data	Validation data	Test data	Epoch
2	2.597	4.551	4.977	31	3.221	7.502	3.222	44
3	1.540	2.900	3.210	30	1.805	6.623	2.896	38
4	0.998	2.089	2.224	27	0.707	5.090	1.726	38
5	0.584	1.655	1.816	24	0.579	4.210	1.315	35
6	0.384	1.055	1.316	23	0.556	4.089	1.300	30
7	0.302	1.254	1.488	21	0.446	4.997	1.750	27
8	0.225	1.887	1.907	18	0.387	6.889	2.870	21

structure of the Nu_f and Nu_r models. For the ANN structure of the ΔP models in forward and reverse directions (Table 16), the number of neurons in the hidden layer is set at 6 and 5, respectively. According to the tables, increasing the number of neurons did not significantly impact the results and only increased the complexity of the system. Nevertheless, as the number of neurons exceeds 7, there's a decline in the RMSE values of the training data, suggesting an improvement in model accuracy. Conversely, the RMSE for the validation and test datasets rises, suggesting a divergence and poor fit of the data. Enhancing the RMSE values of the training data entails sacrificing others, specifically, the risk of overfitting to the training data.

Upon confirming the precision of the ANN models, the derived polynomial models are employed within a Pareto-based multi-objective optimization strategy to identify the optimal combinations of various responses. Fig. 10 represents the multi-objective optimal points for different responses. Considering that in MCHSs, higher thermal performance and lower pressure drop (better hydraulic performance) are considered, in the Pareto diagrams, the Nusselt number is maximized, and the pressure drop is minimized. Fig. 10a is presented for the heat sink in which the flow direction is forward, while Fig. 10b is allocated to the device with reverse movement of the coolant. The states of the most suitable designs and results are shown in these figures as well. It is observable from Fig. 10c that when REI_r enhances, REI_f decreases. It means that if the desired response is REI_r and the goal is to increase this parameter in the heat sink, REI will be lost in the forward direction. For example, if REI increases from 1.525 to 1.573 in the reverse direction, only 0.6 % of the REI_f decreases. Whereas, to improve the REI_f by this percentage, approximately 5 % of the REI_r should be lost. Thus, in the investigated MCHS, increasing the device's overall performance in the reverse direction rather than in the forward direction is much more beneficial. The reason for this issue, as mentioned before, is that inspired by Tesla valves, fins have been placed inside the microchannels so that in the reverse direction, the fluid flow cannot easily pass through the heat sink and has multiple collisions with the fins. Consequently, more wakes are generated in the fluid flow path, leading to increased convective heat transfer. Additionally, more fluid collisions with obstacles optimize the use of the heat transfer surface created by the fins. It should be noted that these collisions significantly increase the ΔP_r. However, in the forward direction, the path is designed in such a way that the fluid can easily pass through the obstacles with less pressure drop. In this case, smaller wakes are generated compared to the reverse direction, which also provides less convective heat transfer. Fig. 10d shows the points with maximum Δp_r value and minimum Δp_f value. If it is necessary to use the device as a one-way valve temporarily, this data can be used. There is no dominance between the points, indicating that there are no two points where one response matches while the other differs. In simpler terms, transitioning from one point to another inevitably results in an improvement in one response and a decline in the other.

Eventually, eight different optimal settings based on the optimum values for the input variables of α, β, and R are derived from these multi-objective optimal points. To perform this optimization, the obtained ANN models and the GA method have been used. Table 17 introduces predicted optimum settings for eight different conditions. This table declares that if the goal is to reach the maximum Nu_f, the configurations of Setting 1 should be used. In Setting 1, the input variables of α, β, and R have the optimum values of 60, 140, and 80 μm, respectively. Tables 18 and 19 represent the anticipated values of results by ANN models and the simulated data for each setting, respectively. The REI value for each forward and reverse direction shows how much the heat transfer is worth compared to the occurred pressure drop. The highest values of REI in each direction reveal that the device has superior overall performance in that direction, and the ratio of heat transfer to pressure drop is cost-effective. Setting 2 explains that when the variables of $\alpha = 60$, $\beta = 180$, and $R = 80$ μm are exerted in the manufacturing of these fins, the maximum REIR with the value of 1.121 is acquired. This means that reversing the flow direction causes an approximately 12.1 % improvement in the device's overall performance. Besides, the overall performance of the heat sink when using the configuration of Setting 2 in fin production has improved by 57.1 % com-

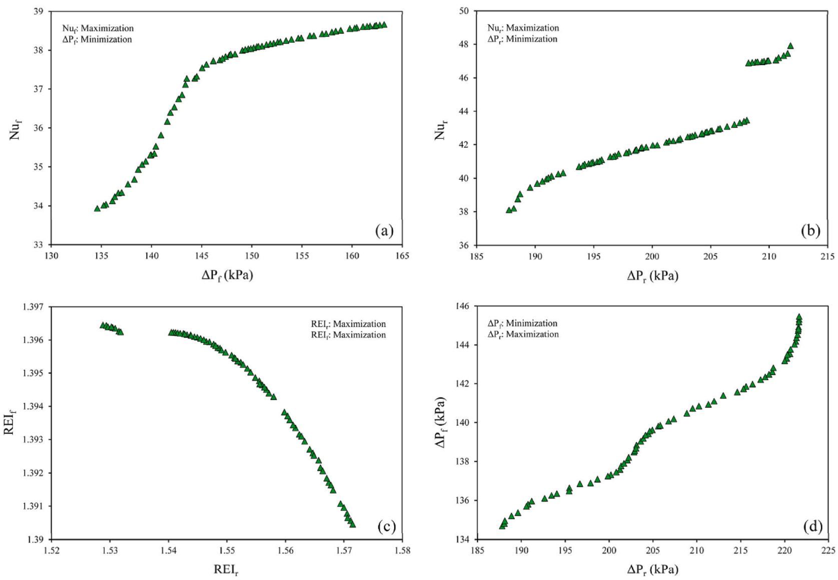

Fig. 10. Multi-objective optimal points for (a) Nu_f and ΔP_f, (b) Nu_r and ΔP_r, (c) REI_r and REI_f, and (d) ΔP_r and ΔP_f.

Table 17
Predicted optimum settings for different conditions.

Optimized parameter	Optimization mode	Optimal setting name	ANN		
			α (degree)	β (degree)	R (μm)
Nu_f	Maximization	Setting 1	60	140	80
Nu_r	Maximization	Setting 2	60	180	80
ΔP_f	Minimization	Setting 3	30	180	40
ΔP_r	Minimization	Setting 4	31.05	180	40
$\mathrm{REI_f}$	Maximization	Setting 5	60	152.32	73.10
$\mathrm{REI_r}$	Maximization	Setting 2	60	180	80
REIR	Maximization	Setting 2	60	180	80
Di	Maximization	Setting 6	46.17	180	73.20

Table 18
The values of results predicted by ANN models.

Optimal setting name	The anticipated results through ANN models							
	Nu_f	Nu_r	ΔP_f (kPa)	ΔP_r (kPa)	$\mathrm{REI_f}$	$\mathrm{REI_r}$	REIR	Di
Setting 1	38.659	46.763	163.458	208.905	1.378	1.536	1.115	1.278
Setting 2	38.135	48.080	152.797	211.552	1.390	1.572	1.131	1.385
Setting 3	33.921	38.021	134.546	187.799	1.290	1.294	1.003	1.396
Setting 4	33.963	38.172	134.599	187.072	1.291	1.299	1.006	1.395
Setting 5	37.959	46.769	148.527	211.741	1.397	1.529	1.094	1.426
Setting 6	36.457	45.106	143.425	220.534	1.357	1.455	1.072	1.538

Table 19
The values of results obtained from numerical simulation.

Optimal setting name	The simulated results through the numerical method							
	Nu_f	Nu_r	ΔP_f (kPa)	ΔP_r (kPa)	$\mathrm{REI_f}$	$\mathrm{REI_r}$	REIR	Di
Setting 1	38.654	47.000	163.460	208.900	1.377	1.542	1.120	1.278
Setting 2	38.453	48.066	152.800	211.700	1.401	1.571	1.121	1.385
Setting 3	33.920	38.003	134.130	187.180	1.291	1.294	1.002	1.396
Setting 4	33.654	38.372	134.320	188.550	1.280	1.304	1.018	1.404
Setting 5	38.470	47.213	150.020	209.500	1.411	1.549	1.098	1.397
Setting 6	36.612	45.463	143.740	217.530	1.362	1.473	1.081	1.513

pared to the performance of the system with no fins. In Setting 2, the highest cooling performance has been achieved with the least possible pressure drop, resulting in a 57.1 % improvement in efficiency compared to the same heat sink in a configuration without fins. The advancement of MCHSs, as exemplified by the achievement in Setting 2, holds significant implications for various applications, particularly in the cooling systems of servers, CPUs, and GPUs. These components are crucial for modern computing systems, where efficient heat dissipation is essential for optimal performance and longevity. The significant improvement achieved in Setting 2 highlights the immense potential of using MCHSs with Tesla valve-shaped fins to enhance the cooling performance of the microelectronic devices. As technology continues to advance, the adoption of these innovative thermal management solutions is poised to play a vital role in shaping the future of electronic devices and computing systems. Considering the diodicity values, Setting 6 reports that with the input variables of $\alpha = 46.17$, $\beta = 180$, and $R = 73.20$ μm, the MCHS reaches the maximum diodicity with the value of 1.513. This explains that when the direction changes to reverse, the pressure drop rises by about 51.3 %. To switch the flow direction in microelectronic systems, one can use a central reversible pump that is programmed to adjust the flow direction according to the requirements. By changing the pump's operating mode, the flow direction can be reversed as needed to optimize heat dissipation. Alternatively, one can manually change the flow direction into the heat sink. Installing valves at strategic points in the cooling system enables manual or automated control of flow direction.

After obtaining the optimal design (Setting 2), a study for different Re between 100 and 500 conducted. Table 20 indicates the values of the investigated metrics for various Re. As can be observed, with an enhance in the Re, the Nusselt number increases, and consequently, the pressure drop increases. However, according to the REI, it becomes clear to what extent increasing the Nu and ΔP is reasonable and logical compared to the base case. It is observed that up to a Re of 300, the values of REI increase in both forward and reverse directions. For example, at a Re of 300, the overall performance of the system in the reverse direction is enhanced by about 58.9 % compared to the base case. However, at Re above 300, the values of REI decrease in both directions. This signifies that the performance of the introduced system is better up to a Re of 300 compared to the base case, and it weakens afterward. According to the table, the values of REIR indicate how the system performs in the reverse mode compared to the forward mode at each Re. It is noticed that with an increase in the Re up to 200, the value of the RIER increases, and then it decreases. In other words, at a Re of 200, the performance of the heat sink with the optimal design in the reverse mode is better than the forward mode, and after Re 200, the perfor-

Table 20
The results of the Setting 2 design (optimal design) in different Reynolds numbers.

Re	*U* (m/s)	Nu_f	Nu_r	ΔP_f (kPa)	ΔP_r (kPa)	REI_f	REI_r	REIR	*Di*
100	1.176	20.633	24.033	50.390	62.220	1.114	1.209	1.086	1.235
200	2.350	38.453	48.066	152.800	211.700	1.401	1.571	1.121	1.385
300	3.527	57.943	71.692	317.900	458.400	1.436	1.589	1.107	1.442
400	4.703	76.906	96.132	551.600	805.100	1.412	1.556	1.102	1.460
500	5.878	98.368	120.852	855.100	1251.800	1.411	1.532	1.086	1.464

mance of the reverse mode compared to the forward mode weakens. Taking into account the values of diodicity, it is observed that with an increase in the *Re*, the Di value also increases, and ultimately it remains constant at 1.4.

3.4. A comparison between the findings of the suggested design and the other studies

Table 21 compares the outcomes of the present research and the other published research. As can be observed, the proposed design in the present study (Setting 2) provides higher *Nu* and greater heat transfer characteristics than the designs suggested in other published works. This implies significantly better thermal behavior of the system. Due to the lower dimensions and geometry of the microchannels employed herein, the ΔP values are also higher. As mentioned earlier, whether the obtained heat transfer justifies the ΔP incurred is determined by the specific value of the *REI* parameter. By comparing the values of the *REI*, it can be observed that in the proposed design, the overall performance has amended by about 57 % compared to the base case. However, in the work of Wang et al. [69], a 56 % improvement in overall performance was achieved, but the *Nu* obtained in their study is much lower than the value obtained in the current work. This indicates that although the overall performance of the system has improved compared to its base case, it still exhibits lower performance compared to the recent work. This suggests that it may function less effectively in electronic equipment cooling, highlighting the importance of the findings in the present study. According to the table, the dimensions of the channels and the flow rates in the current work are relatively small compared to other studies, underscoring the importance of obtaining the reported results with these modest values.

4. Conclusions

Inspiring the structure of the Tesla valves, several fins were designed to be added within the channels of an MCHS. The application of these fins within the microchannels made the channels act like a Tesla valve, resulting in a distinct ΔP and heat transfer in the forward and reverse directions. Four ANNs were exerted to anticipate the Nu_f, Nu_r, ΔP_f, and ΔP_r. The acute angle of the divider (α), the obtuse angle of the divider (β), and the radius of the divider (R) were changed to reach the best fins' configuration. The obtained results indicated that.

- By applying Tesla valve-shaped fins, the total performance of the MCHS was amended in both forward and reverse directions compared to the case without fins.
- In all cases, the diodicity parameter with values higher than 1 indicated that the application of these fins within the microchannels resulted in a higher ΔP_r. This work aimed to change the flow direction whenever a lower ΔP alongside a high heat transfer is needed.
- The prediction models obtained by the ANN method had high accuracy for each response ($R^2 = 0.99$).
- If the goal was to increase the overall performance of the heat sink in the reverse direction, Setting 2 was proposed, in which the overall performance of the system improved by about 57.1 % compared to the fin-less MCHS.
- Implementing the parameters of Setting 5 ($\alpha = 60$ $\beta = 152.32$, and $R = 73.10$ μm) during fin production resulted in a notable enhancement of about 41.1 % in the device's overall performance.
- Setting 6 had a significant increase in diodicity, rising by approximately 51.3 % when utilizing MCHS with input variables of $\alpha = 46.17$, $\beta = 180$, and $R = 73.20$ μm.

Table 21
The findings of the present research and the other published investigations.

Study	MCHS design	Dimension of channel (μm)	*Re*	*Nu*	ΔP (kPa)	*REI*
Present work	Setting 2 (Reverse flow)	300 × 50	200	48.066	211.700	1.571
Present work	Setting 2 (Forward flow)	300 × 50	200	38.453	152.800	1.401
Vaferi et al. [32]	Disk-shaped MCHS with cavities	600 × 500	1000	19.176	5.760	1.070
Elboughdiri et al. [70]	MCHS with arc-curved channels	713 × 231	200	29.118	9.095	1.219
Xie et al. [71]	Disk-shaped MCHS with baffles	1000 × 500	500	40.404	6.355	1.273
Bhandari et al. [72]	MCHS with rectangular fins	9000 × 2000	200	22.550	0.030	0.960
Shuqi et al. [73]	Rectangular-shaped MCHS with baffles	5020 × 1500	1000	81.303	0.525	1.460
Cao et al. [74]	MCHS with rectangular channels and fins	713 × 231	200	25.498	76.488	1.334
Zheng et al. [75]	Pin-fin MCHS	500 × 350	1500	13.8	5.550	1.025
Liang et al. [76]	MCHS with rectangular channels and fins	300 × 50	300	39.115	51.200	1.375
Wang et al. [69]	MCHS with ribs	300 × 100	200	11.800	0.740	1.568
Okab et al. [19]	MCHS with fins	2750 × 1000	200	10	0.200	1.120

Here, the future scopes of the current research are also presented.

- Using acoustic waves to create mixing within the fluid and enhance convection.
- Utilizing the Electrohydrodynamics (EHD) method to enhance heat transfer performance.
- Using nanofluids instead of the conventional fluids within the device.
- Creating modifications in the geometry of microchannels and fins to enhance the overall performance of the heat sink.

CRediT authorship contribution statement

Longyi Ran: Supervision, Conceptualization. **Samah G. Babiker:** Project administration, Funding acquisition. **Pradeep Kumar Singh:** Methodology, Formal analysis. **Mohammed A. Alghassab:** Investigation, Formal analysis. **Ngoc Vu-Thi-Minh:** Resources, Data curation. **Myasar mundher adnan:** Writing – review & editing, Resources. **Salah Knani:** Resources, Project administration, Funding acquisition. **Hakim AL Garalleh:** Writing – original draft, Data curation. **Albara Ibrahim Alrawashdeh:** Validation, Investigation. **Fawaz S. Alharbi:** Writing – original draft, Resources. **Hadil faris Alotaibi:** Writing – review & editing, Project administration, Funding acquisition. **Fahid Riaz:** Writing – review & editing, Writing – original draft.

Declaration of competing interest

The authors declare that they have no known competing financial interests or personal relationships that could have appeared to influence the work reported in this paper.

Acknowledgement

The authors extend their appreciation to the Deanship of Scientific Research at Northern Border University, Arar, KSA for funding this research work through the project number “NBU-FFR-2024-2483-05". This work was supported by Princess Nourah bint Abdulrahman University researchers supporting project number (PNURSP2024R205), Princess Nourah bint Abdulrahman University, Riyadh, Saudi Arabia The author extend their appreciation to the deanship of scientific research at Shaqra university for support this research work. This work was supported by Chongqing Education Commission Science and Technology Research Project (KJQN202204504). This research was supported by the research program by Foreign Trade University (grant number FTURP02-2020-16).

Data availability

The authors do not have permission to share data.

References

[1] R. Wrobel, R.J. McGlen, Heat pipes in thermal management of electrical machines – a review, Therm. Sci. Eng. Prog. 26 (2021) 101053, https://doi.org/10.1016/j.tsep.2021.101053.
[2] Z. Zeng, D. Cao, H. Dong, W. Zhang, X. Li, Cooling/heating dual-stage actuators decoupling structure design and energy management strategy for thermostatic airflow control, Therm. Sci. Eng. Prog. 39 (2023) 101723, https://doi.org/10.1016/j.tsep.2023.101723.
[3] F. Su, X. He, M. Dai, J. Yang, A. Hamanaka, Y. Yu, W. Li, J. Li, Estimation of the cavity volume in the gasification zone for underground coal gasification under different oxygen flow conditions, Energy 285 (2023) 129309, https://doi.org/10.1016/j.energy.2023.129309.
[4] A. Moradikazerouni, Experimental and numerical investigation of traveling wave tube radial heat sink connector thermal stress and deformation with a focus on energy cost management, Int. Commun. Heat Mass Tran. 131 (2022) 105770, https://doi.org/10.1016/j.icheatmasstransfer.2021.105770.
[5] Y. Fu, B. Bian, Y. Liu, L. Zhang, M. Li, J. Wen, G. Xu, Airside heat transfer analysis using Wilson plot method of three analogous serpentine tube heat exchangers for aero-engine cooling, Appl. Therm. Eng. 248 (2024) 123238, https://doi.org/10.1016/j.applthermaleng.2024.123238.
[6] D.B. Tuckerman, R.F.W. Pease, High-performance heat sinking for VLSI, IEEE Electron. Device Lett. 2 (1981) 126–129, https://doi.org/10.1109/EDL.1981.25367.
[7] H. Rostamzadeh, M. Feili, H. Ghaebi, Double-flash enhanced Kalina-based binary geothermal power plants, in: Thermodyn. Anal. Optim. Geotherm. Power Plants, Elsevier, 2021, pp. 167–184, https://doi.org/10.1016/B978-0-12-821037-6.00009-3.
[8] Y.-H. Pan, R. Zhao, Y.-L. Nian, W.-L. Cheng, Numerical study on heat transfer characteristics of a pin–fin staggered manifold microchannel heat sink, Appl. Therm. Eng. 219 (2023) 119436, https://doi.org/10.1016/j.applthermaleng.2022.119436.
[9] H.M. Maghrabie, A.G. Olabi, E.T. Sayed, T. Wilberforce, K. Elsaid, M.H. Doranehgard, M.A. Abdelkareem, Microchannel heat sinks with nanofluids for cooling electronic components: performance enhancement, challenges, and limitations, Therm. Sci. Eng. Prog. 37 (2023) 101608, https://doi.org/10.1016/j.tsep.2022.101608.
[10] K. Fu, W. Gao, X. Xu, X. Liang, Flow boiling heat transfer and pressure drop characteristics of water in a copper foam fin microchannel heat sink, Appl. Therm. Eng. 218 (2023) 119295, https://doi.org/10.1016/j.applthermaleng.2022.119295.
[11] K. Vaferi, M. Vajdi, S. Nekahi, S. Nekahi, F. Sadegh Moghanlou, S. Azizi, M. Shahedi Asl, Numerical simulation of cooling performance in microchannel heat sinks made of AlN ceramics, Microsyst. Technol. (2022), https://doi.org/10.1007/s00542-022-05400-x.
[12] N. Ali, S. Srivastava, I. Haque, J. Yadav, T. Alam, T.U. Siddiqui, M.I.H. Siddiqui, E. Cuce, Heat dissipation and fluid flow in micro-channel heat sink equipped with semi-elliptical pin-fin structures: a numerical study, Int. Commun. Heat Mass Tran. 155 (2024) 107492, https://doi.org/10.1016/j.icheatmasstransfer.2024.107492.
[13] I. Haque, T. Alam, J. Yadav, N.K. Gupta, M.I. Haque Siddiqui, T.U. Siddiqui, N. Ali, S. Srivastava, A.S. Yadav, A. Sharma, R. Khargotra, A.K. Thakur, Numerical analysis of various shapes of lozenge pin-fins in microchannel heat sink, Int. J. Chem. React. Eng. 22 (2024) 31–43, https://doi.org/10.1515/ijcre-2023-0092.
[14] M. Yang, B.-Y. Cao, Multi-objective optimization of a hybrid microchannel heat sink combining manifold concept with secondary channels, Appl. Therm. Eng. 181 (2020) 115592, https://doi.org/10.1016/j.applthermaleng.2020.115592.
[15] K. Lu, C. Wang, H. He, X. Fan, F. Chen, F. Qi, C. Wang, Numerical simulation and experimental investigation on heat transfer and hydraulic characteristics of rectangular microchannel heat sinks using high thermal conductivity diamond/copper composites, Diam. Relat. Mater. 147 (2024) 111371, https://doi.org/10.1016/j.diamond.2024.111371.
[16] F. Zhang, B. Wu, B. Du, Heat transfer optimization based on finned microchannel heat sink, Int. J. Therm. Sci. 172 (2022) 107357, https://doi.org/10.1016/

j.ijthermalsci.2021.107357.
[17] R. Singupuram, T. Alam, M.A. Ali, S. Shaik, N.K. Gupta, N. Akkurt, M. Kumar, S.M. Eldin, D. Dobrotă, Numerical analysis of heat transfer and fluid flow in microchannel heat sinks for thermal management, Case Stud. Therm. Eng. 45 (2023) 102964, https://doi.org/10.1016/j.csite.2023.102964.
[18] M.E. Polat, F. Ulger, S. Cadirci, Multi-objective optimization and performance assessment of microchannel heat sinks with micro pin-fins, Int. J. Therm. Sci. 174 (2022) 107432, https://doi.org/10.1016/j.ijthermalsci.2021.107432.
[19] A.K. Okab, H.M. Hasan, M. Hamzah, K. Egab, A. Al-Manea, T. Yusaf, Analysis of heat transfer and fluid flow in a microchannel heat sink with sidewall dimples and fillet profile, Int. J. Thermofluids 15 (2022) 100192, https://doi.org/10.1016/j.ijft.2022.100192.
[20] A. Dash, T. Alam, M. Siddiqui, P. Blecich, M. Kumar, N. Gupta, M. Ali, A. Yadav, Impact on heat transfer rate due to an extended surface on the passage of microchannel using cylindrical ribs with varying sector angle, Energies 15 (2022) 8191, https://doi.org/10.3390/en15218191.
[21] S. Saha, T. Alam, M.I.H. Siddiqui, M. Kumar, M.A. Ali, N.K. Gupta, D. Dobrotă, Analysis of microchannel heat sink of silicon material with right triangular groove on sidewall of passage, Materials 15 (2022) 7020, https://doi.org/10.3390/ma15197020.
[22] A. Vatsa, T. Alam, M.I.H. Siddiqui, M.A. Ali, D. Dobrotă, Performance of microchannel heat sink made of silicon material with the two-sided wedge, Materials 15 (2022) 4740, https://doi.org/10.3390/ma15144740.
[23] M. Feili, M. Hasanzadeh, H. Ghaebi, E. Abdi Aghdam, Comprehensive analysis of a novel cooling/electricity cogeneration system driven by waste heat of a marine diesel engine, Energy Sources, Part A Recover. Util. Environ. Eff. 44 (2022) 7331–7346, https://doi.org/10.1080/15567036.2022.2108167.
[24] Q. Mei, L. Liu, M.R. Abu Mansor, Investigation on spray combustion modeling for performance analysis of future low- and zero-carbon DI engine, Energy 302 (2024) 131906, https://doi.org/10.1016/j.energy.2024.131906.
[25] W. Liao, D. Jing, Experimental study on fluid mixing and pressure drop of mini-mixer with flexible vortex generator, Int. Commun. Heat Mass Tran. 142 (2023) 106615, https://doi.org/10.1016/j.icheatmasstransfer.2023.106615.
[26] F. Chen, Z. Jin, Effects of perforated plate on hydrogen flow in L-shaped high pressure reducing valve, Int. J. Hydrogen Energy 48 (2023) 1956–1967, https://doi.org/10.1016/j.ijhydene.2022.09.276.
[27] A. Farajollahi, M. Rostami, M. Feili, H. Ghaebi, Thermodynamic and economic evaluation and optimization of the applicability of integrating an innovative multi-heat recovery with a dual-flash binary geothermal power plant, Clean Technol. Environ. Policy 25 (2023) 1673–1698, https://doi.org/10.1007/s10098-023-02465-8.
[28] C. Lai, S. Shan, S. Feng, Y. Chen, J. Zeng, J. Song, L. Fu, Numerical investigations on heat transfer enhancement and energy flow distribution for interlayer battery thermal management system using Tesla-valve mini-channel cooling, Energy Convers. Manag. 280 (2023) 116812, https://doi.org/10.1016/j.enconman.2023.116812.
[29] F. Gong, X. Yang, X. Zhang, Z. Mao, W. Gao, C. Wang, The study of Tesla valve flow field on the net power of proton exchange membrane fuel cell, Appl. Energy 329 (2023) 120276, https://doi.org/10.1016/j.apenergy.2022.120276.
[30] M.C. Constantino, F.T. Kanizawa, Evaluation of pressure drop effect on COP of single-stage vapor compression refrigeration cycles, Therm. Sci. Eng. Prog. 28 (2022) 101048, https://doi.org/10.1016/j.tsep.2021.101048.
[31] B.S. Onal, S.M. Kirkar, D. Akgul, A. Celen, O. Acikgoz, A.S. Dalkilic, S.N. Kazi, S. Wongwises, Heat transfer and pressure drop characteristics of two phase flow in helical coils, Therm. Sci. Eng. Prog. 27 (2022) 101143, https://doi.org/10.1016/j.tsep.2021.101143.
[32] K. Vaferi, M. Vajdi, S. Nekahi, A. Heydari, F. Sadegh Moghanlou, H. Nami, H. Jafarzadeh, Thermo-hydraulic performance optimization of a disk-shaped microchannel heat sink applying computational fluid dynamics, artificial neural network, and response surface methodology, Heliyon 9 (2023) e21031, https://doi.org/10.1016/j.heliyon.2023.e21031.
[33] H. Hu, I. Son, H. Kikumoto, B. Zhang, K. Hayashi, Improving Tesla valve shape within fluid diode plates for building ventilation, Build. Environ. 252 (2024) 111259, https://doi.org/10.1016/j.buildenv.2024.111259.
[34] J. Xiang, J. Liu, W. Yang, X. Wei, P. Li, Z. Chen, Y. Zheng, J. Huang, Development of novel thermal diode based on improved check valve and modified wick structure, Int. J. Therm. Sci. 200 (2024) 108977, https://doi.org/10.1016/j.ijthermalsci.2024.108977.
[35] Y. Hou, M. Cheng, Z. Sheng, J. Wang, Unsteady conjugate heat transfer simulation of wall heat loads for rotating detonation combustor, Int. J. Heat Mass Tran. 221 (2024) 125081, https://doi.org/10.1016/j.ijheatmasstransfer.2023.125081.
[36] Y. Zhang, S. He, X. Jiang, Z. Wang, Y. Wang, M. Gu, X. Yang, S. Zhang, J. Cao, H. Fang, Q. Li, Performance and configuration optimization of proton exchange membrane fuel cell considering dual symmetric Tesla valve flow field, Energy 288 (2024) 129791, https://doi.org/10.1016/j.energy.2023.129791.
[37] H. Guo, S. Tian, L. Wang, C. Xiao, S. Yang, Numerical study of Tesla valve flow field on proton exchange membrane fuel cell performance, Int. J. Hydrogen Energy 50 (2024) 1573–1583, https://doi.org/10.1016/j.ijhydene.2023.11.108.
[38] S. Nekahi, F. Sadegh Moghanlou, K. Vaferi, H. Ghaebi, M. Vajdi, H. Nami, Optimizing finned-microchannel heat sink design for enhanced overall performance by three different approaches: numerical simulation, artificial neural network, and multi-objective optimization, Appl. Therm. Eng. 245 (2024) 122835, https://doi.org/10.1016/j.applthermaleng.2024.122835.
[39] L. Sun, J. Li, H. Xu, J. Ma, H. Peng, Numerical study on heat transfer and flow characteristics of novel microchannel heat sinks, Int. J. Therm. Sci. 176 (2022) 107535, https://doi.org/10.1016/j.ijthermalsci.2022.107535.
[40] X. Zhang, Z. Cao, K. Fang, X. Yang, Study on the influence of different structural parameters on the performance of Tesla valve, J. Phys. Conf. Ser. 2707 (2024) 012092, https://doi.org/10.1088/1742-6596/2707/1/012092.
[41] Y. Fan, Z. Wang, X. Xiong, J. Zhu, Q. Gao, H. Wang, H. Wu, Novel concept design of low energy hybrid battery thermal management system using PCM and multistage Tesla valve liquid cooling, Appl. Therm. Eng. 220 (2023) 119680, https://doi.org/10.1016/j.applthermaleng.2022.119680.
[42] P. Li, Y. Liu, Q. Wen, Z. Zhang, Y. Ma, J. Zhu, Optimization of multi-staged Tesla valve using response surface methodology, Phys. Fluids 36 (2024), https://doi.org/10.1063/5.0200342.
[43] W. Sun, X. Zhang, B. Liu, L. Zhao, Q. Cheng, Z. Wang, Analysis of the main influencing factors of waste heat utilization effectiveness in the tank storage receiving process of waxy crude oil under dynamic liquid level conditions, Renew. Energy 228 (2024) 120707, https://doi.org/10.1016/j.renene.2024.120707.
[44] C. Zhu, M. Wang, M. Guo, J. Deng, Q. Du, W. Wei, Y. Zhang, S.S. Ashraf Talesh, Optimizing solar-driven multi-generation systems: a cascade heat recovery approach for power, cooling, and freshwater production, Appl. Therm. Eng. 240 (2024) 122214, https://doi.org/10.1016/j.applthermaleng.2023.122214.
[45] S. Nekahi, K. Vaferi, S. Nekahi, M. Vajdi, F. Sadegh Moghanlou, N. Baydogan, M.S. Asl, Finned heat exchangers made of TiB2–SiC–graphene composites with enhanced heat transfer performance, J. Brazilian Soc. Mech. Sci. Eng. 45 (2023) 497, https://doi.org/10.1007/s40430-023-04362-z.
[46] N.B. Shaik, M. Inayat, W. Benjapolakul, B. Bakthavatchalam, S.D. Barewar, W. Asdornwised, S. Chaitusaney, Artificial neural network modeling and optimization of thermophysical behavior of MXene Ionanofluids for hybrid solar photovoltaic and thermal systems, Therm. Sci. Eng. Prog. 33 (2022) 101391, https://doi.org/10.1016/j.tsep.2022.101391.
[47] C. Li, F. Ye, R. Chahine, T. Yang, J. Xiao, Genetic algorithm optimized artificial neural network models of single- and multi-component gas adsorption isotherms for hydrogen purification, Int. J. Hydrogen Energy 52 (2024) 1127–1142, https://doi.org/10.1016/j.ijhydene.2023.04.352.
[48] F. Li, T.C.A. Kumar, Y. Elmasry, P.K. Singh, A.M. Abed, A.D. Algarni, V.N. Nguyen, M. Wae-hayee, P.Q. Phong Nguyen, A.M. Galal, Response Surface Methodology and Artificial Neural Network modellings on hydraulic and thermal performances of a disk-shaped heat sink with tree-like microchannels, Case Stud. Therm. Eng. 40 (2022) 102539, https://doi.org/10.1016/j.csite.2022.102539.
[49] K. Vaferi, M. Vajdi, A. Shadian, H. Ahadnejad, F.S. Moghanlou, H. Nami, H. Jafarzadeh, Modeling and optimization of hydraulic and thermal performance of a tesla valve using a numerical method and artificial neural network, Entropy 25 (2023) 967, https://doi.org/10.3390/e25070967.
[50] C. Xie, G. Yan, Q. Ma, Y. Elmasry, P.K. Singh, A.M. Algelany, M. Wae-hayee, Flow and heat transfer optimization of a fin-tube heat exchanger with vortex generators using Response Surface Methodology and Artificial Neural Network, Case Stud. Therm. Eng. 39 (2022) 102445, https://doi.org/10.1016/j.csite.2022.102445.
[51] C. Kou, M.A. Alghassab, A.M. Abed, S. Alkhalaf, F.S. Alharbi, Y. Elmasry, S. Abdullaev, H. AL Garalleh, M.A. Tarawneh, Modeling of hydrogen flow decompression from a storage by a two-stage Tesla valve: a hybrid approach of artificial neural network, response surface methodology, and genetic algorithm optimization, J. Energy Storage 85 (2024) 111104, https://doi.org/10.1016/j.est.2024.111104.
[52] N. Tran, Y.-J. Chang, J. Teng, T. Dang, R. Greif, Enhancement thermodynamic performance of microchannel heat sink by using a novel multi-nozzle structure,

Int. J. Heat Mass Tran. 101 (2016) 656–666, https://doi.org/10.1016/j.ijheatmasstransfer.2016.04.111.
[53] Y. Bao, H. Wang, Numerical study on flow and heat transfer characteristics of a novel Tesla valve with improved evaluation method, Int. J. Heat Mass Tran. 187 (2022) 122540, https://doi.org/10.1016/j.ijheatmasstransfer.2022.122540.
[54] Y.-M. Hwang, C.-T. Pan, B.-S. Chen, S.-R. Jian, Numerical analysis of the welding behaviors in micro-copper bumps, Metals 11 (2021) 460, https://doi.org/10.3390/met11030460.
[55] S. Sabzpoushan, M. Sabouri, Secondary flow through lateral passages to improve hydrothermal performance of liquid-cooled microchannel heat sinks, Appl. Therm. Eng. (2023) 120009, https://doi.org/10.1016/j.applthermaleng.2023.120009.
[56] C. Zhu, M. Wang, M. Guo, J. Deng, Q. Du, W. Wei, Y. Zhang, A. Mohebbi, An innovative process design and multi-criteria study/optimization of a biomass digestion-supercritical carbon dioxide scenario toward boosting a geothermal-driven cogeneration system for power and heat, Energy 292 (2024) 130408, https://doi.org/10.1016/j.energy.2024.130408.
[57] D. Chen, S. Serbin, K. Burunsuz, Features of a gas turbine combustion chamber in operation with gaseous ammonia, Fuel 372 (2024) 132149, https://doi.org/10.1016/j.fuel.2024.132149.
[58] J. Qian, M. Chen, Z. Gao, Z. Jin, Mach number and energy loss analysis inside multi-stage Tesla valves for hydrogen decompression, Energy 179 (2019) 647–654, https://doi.org/10.1016/j.energy.2019.05.064.
[59] K. Xu, B. Ruan, H. Meng, A thermal performance factor for evaluation of active engine cooling with asymmetric heating, Appl. Therm. Eng. 73 (2014) 351–356, https://doi.org/10.1016/j.applthermaleng.2014.07.066.
[60] P. Cheng, X. Jianjun, J. Kumar, H. Almujibah, H. Elhosiny Ali, T. Alkhalifah, S. Alkhalaf, F. Alturise, R. Ghandour, Improving efficiency and optimizing heat transfer in a novel tesla valve through multi-layer perceptron models, Case Stud. Therm. Eng. 49 (2023) 103391, https://doi.org/10.1016/j.csite.2023.103391.
[61] W. Qu, I. Mudawar, Experimental and numerical study of pressure drop and heat transfer in a single-phase micro-channel heat sink, Int. J. Heat Mass Tran. 45 (2002) 2549–2565, https://doi.org/10.1016/S0017-9310(01)00337-4.
[62] Y. Di, R. Li, H. Tian, J. Guo, B. Shi, Z. Wang, K. Yan, Y. Liu, A maneuvering target tracking based on fastIMM-extended Viterbi algorithm, Neural Comput. Appl. (2023), https://doi.org/10.1007/s00521-023-09039-1.
[63] R. Prasad, K.D. Yadav, USE of response surface methodology and artificial neural network approach for methylene blue removal by adsorption onto water hyacinth, water conserv, OR Manag. 4 (2020) 83–89, https://doi.org/10.26480/wcm.02.2020.83.89.
[64] G. Sodeifian, Z. Niazi, Prediction of CO2 absorption by nanofluids using artificial neural network modeling, Int. Commun. Heat Mass Tran. 123 (2021) 105193, https://doi.org/10.1016/j.icheatmasstransfer.2021.105193.
[65] A. Filali, L. Khezzar, H. Semmari, O. Matar, Application of artificial neural network for mixed convection in a square lid-driven cavity with double vertical or horizontal oriented rectangular blocks, Int. Commun. Heat Mass Tran. 129 (2021) 105644, https://doi.org/10.1016/j.icheatmasstransfer.2021.105644.
[66] W. Escher, T. Brunschwiler, B. Michel, D. Poulikakos, Experimental investigation of an ultrathin manifold microchannel heat sink for liquid-cooled chips, J. Heat Tran. 132 (2010), https://doi.org/10.1115/1.4001306.
[67] S.P. Shetty, S. Nayak, S. Kumar, K. Vasudeva Karanth, Thermo-hydraulic performance prediction of a solar air heater with circular perforated absorber plate using Artificial Neural Network, Therm. Sci. Eng. Prog. 23 (2021) 100886, https://doi.org/10.1016/j.tsep.2021.100886.
[68] D. Chen, Y. Li, X. Li, X. Hong, X. Fan, T. Savidge, Key difference between transition state stabilization and ground state destabilization: increasing atomic charge densities before or during enzyme–substrate binding, Chem. Sci. 13 (2022) 8193–8202, https://doi.org/10.1039/D2SC01994A.
[69] W. Wang, Y. Li, Y. Zhang, B. Li, B. Sundén, Analysis of laminar flow and heat transfer in an interrupted microchannel heat sink with different shaped ribs, J. Therm. Anal. Calorim. 140 (2020) 1259–1266, https://doi.org/10.1007/s10973-019-09156-x.
[70] N. Elboughdiri, S.Q. Salih, B.S. Chauhan, A. Albani, T.U.K. Nutakki, F. Alturise, S. Alkhalaf, S.M. Siddeeg, A. Deifalla, Arc-curved microchannels engraved on segmented circular heat sink for heat transfer augmentation; ANN-based performance optimization, Case Stud. Therm. Eng. 53 (2024) 103837, https://doi.org/10.1016/j.csite.2023.103837.
[71] Y. Xie, T.U. Kumar Nutakki, D. Wang, X. Xu, Y. Li, M. Nadeem Khan, A. Deifalla, Y. Elmasry, R. Chen, Multi-objective optimization of a microchannel heat sink with a novel channel arrangement using artificial neural network and genetic algorithm, Case Stud. Therm. Eng. 53 (2024) 103938, https://doi.org/10.1016/j.csite.2023.103938.
[72] P. Bhandari, Y.K. Prajapati, Thermal performance of open microchannel heat sink with variable pin fin height, Int. J. Therm. Sci. 159 (2021) 106609, https://doi.org/10.1016/j.ijthermalsci.2020.106609.
[73] Z. Shuqi, Y. Limei, V. Goyal, S. Alghanmi, T. Alkhalifah, S. Alkhalaf, F. Alturise, H. Elhosiny Ali, A. Deifalla, Artificial neural network-based optimization of baffle geometries for maximized heat transfer efficiency in microchannel heat sinks, Case Stud. Therm. Eng. 49 (2023) 103331, https://doi.org/10.1016/j.csite.2023.103331.
[74] Y. Cao, M. Abbas, M.A. El-Shorbagy, K.A. Gepreel, M. Dahari, V.V. Le, M.F. Badran, P.H. Huynh, M. Wae-hayee, Thermo-hydraulic performance in ceramic-made microchannel heat sinks with an optimum fin geometry, Case Stud. Therm. Eng. 36 (2022) 102230, https://doi.org/10.1016/j.csite.2022.102230.
[75] R. Zheng, Y. Wu, Y. Li, G. Wang, G. Ding, Y. Sun, Development of a hierarchical microchannel heat sink with flow field reconstruction and low thermal resistance for high heat flux dissipation, Int. J. Heat Mass Tran. 182 (2022) 121925, https://doi.org/10.1016/j.ijheatmasstransfer.2021.121925.
[76] X. Liang, N.B. Kumar, I.B. Mansir, P. Kumar Singh, A.M. Abed, M. Dahari, S. Nasr, H. Albalawi, A. Cherif, M. Wae-hayee, Management of heat transfer and hydraulic characteristics of a micro-channel heat sink with various arrangements of rectangular vortex generators utilizing artificial neural network and response surface methodology, Case Stud. Therm. Eng. 44 (2023) 102850, https://doi.org/10.1016/j.csite.2023.102850.